

A robust well-balanced finite volume model for shallow water flows with wetting and drying over irregular terrain

Lixiang Song, Jianzhong Zhou^{*}, Jun Guo, Qiang Zou, Yi Liu

School of Hydropower and Information Engineering, Huazhong University of Science and Technology, Wuhan 430074, China

ARTICLE INFO

Article history:

Received 10 October 2010

Received in revised form 22 April 2011

Accepted 23 April 2011

Available online 28 April 2011

Keywords:

Shallow water equations

C-property

Wet/dry fronts

Source terms

Unstructured grid

Dam-break flood

ABSTRACT

An unstructured Godunov-type finite volume model is developed for the numerical simulation of geometrically challenging two-dimensional shallow water flows with wetting and drying over convoluted topography. In the framework of sloping bottom model, a modified formulation of shallow water equations is used to preserve mass conservation during flooding and recession. The key ingredient of the model is the use of this combination of the sloping bottom model and the modified shallow water equations to provide a robust technique for wet/dry fronts tracking and, together with centered discretization of the bed slope source term, to exactly preserve the static flow on irregular topographies. The variable reconstruction technique ensures nonnegative reconstructed water depth and reasonable reconstructed velocity, and the friction terms are solved by semi-implicit scheme that does not invert the direction of velocity components. The robustness and accuracy of the proposed model are assessed by comparing numerical and reference results of extensive test cases. Moreover, the results of a dam-break flooding over real topography are presented to show the capability of the model on field-scale application.

© 2011 Elsevier Ltd. All rights reserved.

1. Introduction

There has been considerable interest, of late years, in modeling shallow water flows on irregular terrain (e.g. floods resulting from dam breaches, heavy rainfall or tsunami; estuarine and coastal flows), much of which has been driven by the limitations in existing models, the potential for an improved flow characterization that is offered by newer models, and the explosion of GIS data resources (e.g. Lidar) that is needed to parameterize two-dimensional models. The two-dimensional shallow water equations (SWEs) are widely accepted to mathematically describe long wave hydrodynamics of such free surface flows when the vertical acceleration of the water particles has a negligible effect on the pressure. Because the analytical solutions for SWEs available in the literatures [40,46,35,2] focus on only a few simple cases and have a seriously restricted application prospect, research on numerical resolution of SWEs has attracted tremendous attention in the last two decades [3–6,8–14,16,17,19–23,26,29–32,34,37,39,42,45,47–52].

There are a variety of numerical methods that can be used to solve the shallow water systems, such as finite difference [12] and finite volume methods [28]. Finite volume methods are generally based on the conservative form of the governing equations,

and solve the discretization formulation in computational meshes. The cell-averaged values are updated in each time step by the numerical fluxes through the interfaces of the meshes. Therefore, mass and momentum are conserved locally, even in the presence of discontinuities. Godunov-type finite volume schemes [41,28], which solve Riemann problems for fluxes estimate and evolve the solution forward in time, have experienced a vigorous development in recent years. Performance including accuracy, efficiency and shock-capturing ability has largely been evaluated through idealized benchmark test cases [8,30] and field-scale shallow flow modeling applications [43,1,48,7,3,21,31,45,22], and results show that Godunov methods excel in this context [5]. A recent study of Gallegos et al. [21] in particular shows that Godunov-based models provide an excellent basis for improved flood inundation modeling in urban areas.

Since Bermudez and Vazquez [9] proposed the ideal of the “exact C-property”, which refers to the ability of a scheme to exactly preserve the stationary steady state, the development of Godunov-type methods for numerical resolution of SWEs with complex source terms has become one of the most important research topics, and several well-balanced methods have been successfully developed in [8,23,3,30,17,39,16,47]. George [23] proposed an augmented Riemann solver in which bottom was taken into account. The solver, which was developed in the framework of wave propagation algorithm [28], can preserve a large class of steady states in one-dimensional applications. Liang and Borthwick [29] derived the pre-balanced SWEs by choosing the water level and discharge

^{*} Corresponding author. Tel.: +86 02 78 7543 127.

E-mail addresses: slx.hust@live.cn (L. Song), jz.zhou@hust.edu.cn (J. Zhou).

as dependent variables, and proposed a scheme for solving the pre-balanced SWEs. However, negative water depth would be produced near the wet/dry fronts, and then artificial modification of flow variables had to be made despite the mass error. To deal with this problem, Liang and Marche [30] proposed the nonnegative reconstruction of water depth, and derived additional source terms, which were introduced to cope with the occurrence of dry areas, for balancing spurious fluxes. As a result, there is no need for modifications of flow variables, and the mass conservation is exactly preserved. The one-dimensional shallow flow model [30] was later extended to two-dimensional and simplified to remove the additional source terms for practical applications by Liang [31]. Begnudelli and Sanders [8] introduced the flux correction terms to preserve the well-balanced property in fully wet cell, whereas the velocity in partially wet cell is set to zero. Therefore, the stationary solutions can be maintained in both fully and partially wet cell when the still steady state is encountered. However, the flux corrections are based on the nodal depth, which is computed by subtracting the nodal bottom from the averaged value of water surface elevations in wetted cells surrounding the node, and unphysical high velocities would be observed due to the flux corrections. This is described as follows.

As shown in Fig. 1, the plotted numbers denote the cell id; the flag *a*, *b*, and *c* denote three edges of cell-18, respectively. Water depths of cells in the left of the line A-A' are assumed to be h_1 , whereas water depths of cell-21 and cell-16 are assumed to be h_2 (h_2 is far less than h_1), and water depths of other cells are assumed to be zero. All velocities are assumed to be zero for simplification. The topography is flat and no friction effect is considered. By using the HLLC solver (see Section 3.3), the mass flux across the interface *a* is proportional to $h_2^{3/2}$, and the normal momentum flux is proportional to h_2^2 . However, the flux corrections across the interface *a* and *b* are approximately proportional to h_1^2 (note that h_2 is far less than h_1). Thus, the ratio between momentum flux and mass flux in cell-18 is proportional to $h_1^2/h_2^{3/2}$. When h_2 is very small but h_1 is not small enough, for example $h_2 = 10^{-5}$ m, $h_1 = 5$ m (wet/dry fronts of a dam-break problem), the ratio become very large, resulting in the unphysical high velocity with a very small depth in cell-18. Furthermore, if the bed of the cell-18 is frictional and the semi-implicit scheme [8,39] is used to treat the friction terms, then the high velocity associated with a very small depth would be finally reduced to a reasonable velocity after the friction

terms treatment. See Section 3.6 for more details. Song et al. [39] proposed the flux correction terms for both fully and partially submerged cells, preserving the well-balanced property without the assumption of a zero velocity in partially submerged cell. The flux corrections are based on the nodal depth, which is computed by subtracting the nodal bottom from the cell-based reconstructed water level at vertex. Therefore, the water depth at a vertex may have multi-values, partially depending on the number of cells surrounding the vertex. So there is no problem of high velocity by using the flux corrections. However, the flux corrections in either side of the edge are computed separately and may be unequal in the unsteady situation, leading to another problem of momentum nonconservation. The development of well-balanced schemes without using additional correction terms on unstructured meshes is a significant task.

The simulation of wetting and drying is one of the central challenges that researchers are tackling [50,4,14,11,8,6,3,30]. In finite volume schemes where the velocity is computed by dividing the discharge per unit width by the depth, unphysical high velocity can be predicted at the rapidly moving wet/dry fronts if no special attention is paid. This, in turn, can lead to predictions of unacceptable negative water depth and numerical instability. Moreover, near the wet/dry interface, where the depth is vanishing, the friction terms may cause the stiff problem and significantly affect the stability of the numerical model [39]. Therefore, it is necessary to employ a robust scheme, such as the semi-implicit scheme [8,39], for friction terms when modeling the real-world shallow flow over irregular terrain.

The main objective of this paper is to develop a robust well-balanced Godunov-type finite volume model for the numerical simulation of geometrically challenging shallow water flows. The unstructured triangular meshes are used to facilitate grid generation when the boundary of computational domain is highly irregular. Sloping bottom model together with volume/free-surface relationships (VFRs) [8] is incorporated into the present scheme to provide an efficient and robust technique to track the stationary or moving wet/dry fronts. The pre-balanced SWEs proposed by Liang and Borthwick [29] are modified to preserve mass conservation in both fully and partially submerged cells during flooding and recession. For fully submerged cell, the bed slope terms are discretized exactly based on the water level at the centroid, and the well-balanced property is preserved without any additional terms, such as flux corrections [8,39] and additional source terms [30]. The variable reconstruction technique ensures nonnegative reconstructed water depth and reasonable reconstructed velocity, thus enhances the robustness of model. The friction terms are treated by semi-implicit scheme [8,39], which does not invert the direction of velocity components and so would benefit model robustness.

This paper is organized as follows: Section 2 presents the governing equations for shallow water flows. In Section 3 we combine the sloping bottom model and Godunov-type finite volume scheme together for resolution the modified SWEs on unstructured meshes. In Section 4, the proposed numerical model is validated against several numerical test problems. Brief conclusions are given in Section 5.

2. Shallow water equations

By assuming a hydrostatic pressure distribution, a small bed slope, a uniform velocity distribution in the vertical direction, and a constant fluid density with free surface and bottom boundaries, the Navier–Stokes equations are integrated over the water depth to obtain the governing equations, two-dimensional depth-averaged SWEs, which approximate the depth and horizontal momentum of the flow as follows:

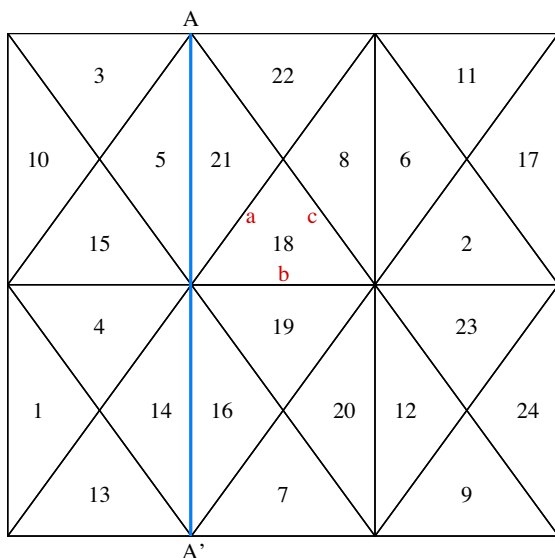


Fig. 1. Schematic diagram of the computational meshes.

$$\frac{\partial \mathbf{U}}{\partial t} + \frac{\partial \mathbf{E}}{\partial x} + \frac{\partial \mathbf{G}}{\partial y} = \mathbf{S}, \quad (1)$$

where t indicates the time; x and y are Cartesian coordinates; \mathbf{U} , \mathbf{E} , \mathbf{G} and \mathbf{S} are vectors of the conserved flow variables, fluxes in the x - and y -directions, and source terms, respectively; in which

$$\mathbf{U} = \begin{bmatrix} h \\ hu \\ hv \end{bmatrix}, \quad \mathbf{E} = \begin{bmatrix} hu \\ hu^2 + gh^2/2 \\ huv \end{bmatrix}, \quad \mathbf{G} = \begin{bmatrix} hv \\ huv \\ hv^2 + gh^2/2 \end{bmatrix},$$

$$\mathbf{S} = \mathbf{S}_0 + \mathbf{S}_f = \begin{bmatrix} 0 \\ ghS_{0x} \\ ghS_{0y} \end{bmatrix} + \begin{bmatrix} 0 \\ -ghS_{fx} \\ -ghS_{fy} \end{bmatrix} \quad (2)$$

where h is the water depth; u and v are the depth-averaged velocity components in the x - and y -directions, respectively; $g = 9.81 \text{ m/s}^2$ is the gravity acceleration; S_{0x} and S_{0y} are bed slopes in the x - and y -directions, respectively; S_{fx} and S_{fy} are friction slopes in the x - and y -directions, respectively. Assume that the bed is fixed, i.e. $b = b(x, y)$, then $S_{0x} = -\partial b / \partial x$ and $S_{0y} = -\partial b / \partial y$. In this paper, the friction slopes are estimated by using the Manning formulae

$$S_{fx} = \frac{n^2 u \sqrt{u^2 + v^2}}{h^{4/3}}, \quad S_{fy} = \frac{n^2 v \sqrt{u^2 + v^2}}{h^{4/3}}, \quad (3)$$

where n is the empirical Manning coefficient that is an estimated parameter reflecting the roughness of the bottom. One of the main reasons for adopting the conservative form of the SWEs is that the resulting numerical models behave better than the primitive form when used to simulate flows with shocks, such as dam-break flows.

By introducing a new variable, η , which denotes the water surface elevation, the SWEs given by (1) and (2) will be transformed into a well-balanced formulation [29] constituted by (1) and

$$\mathbf{U} = \begin{bmatrix} \eta \\ hu \\ hv \end{bmatrix}, \quad \mathbf{E} = \begin{bmatrix} hu \\ hu^2 + g(\eta^2 - 2\eta b)/2 \\ huv \end{bmatrix},$$

$$\mathbf{G} = \begin{bmatrix} hv \\ huv \\ hv^2 + g(\eta^2 - 2\eta b)/2 \end{bmatrix},$$

$$\mathbf{S} = \mathbf{S}_0 + \mathbf{S}_f = \begin{bmatrix} 0 \\ g\eta S_{0x} \\ g\eta S_{0y} \end{bmatrix} + \begin{bmatrix} 0 \\ -ghS_{fx} \\ -ghS_{fy} \end{bmatrix}. \quad (4)$$

The main advantages of the SWEs given by (1) and (4) are that they preserve strict hyperbolicity and are mathematically balanced for the flux gradients and source terms so that the stationary steady state is automatically maintained for wet-bed cases [29].

Note that $\eta = h + b$. The shallow water system given by (1) and (4) will be transformed into another formulation constituted by (1) and

$$\mathbf{U} = \begin{bmatrix} h \\ hu \\ hv \end{bmatrix}, \quad \mathbf{E} = \begin{bmatrix} hu \\ hu^2 + g(h^2 - b^2)/2 \\ huv \end{bmatrix},$$

$$\mathbf{G} = \begin{bmatrix} hv \\ huv \\ hv^2 + g(h^2 - b^2)/2 \end{bmatrix},$$

$$\mathbf{S} = \mathbf{S}_0 + \mathbf{S}_f = \begin{bmatrix} 0 \\ g(h + b)S_{0x} \\ g(h + b)S_{0y} \end{bmatrix} + \begin{bmatrix} 0 \\ -ghS_{fx} \\ -ghS_{fy} \end{bmatrix}. \quad (5)$$

In the framework of sloping bottom model, the above formulation of the shallow water system not only inherits the advantages of (1) and (4), but also exactly preserves mass conservation property in both fully and partially submerged cells, whereas this is not the case for (1) and (4), see Section 3.1 for details. The mass conservation property of (1) and (5) is obvious since the conservative variable, h , is used to update solutions. The hyperbolic property of (1) and (5) is explained below.

The flux Jacobian for (1) and (5) is given by

$$\mathbf{J} = \frac{\partial(\mathbf{E}n_x + \mathbf{G}n_y)}{\partial \mathbf{U}} = \begin{bmatrix} 0 & n_x & n_y \\ (gh - u^2)n_x - uvn_y & 2un_x + vn_y & un_y \\ -uvn_x + (gh - v^2)n_y & vn_x & un_x + 2vn_y \end{bmatrix}, \quad (6)$$

where n_x and n_y are Cartesian components of the unit vector in the x - and y -directions, respectively. The three eigenvalues of the flux Jacobian are

$$\lambda_1 = un_x + vn_y - \sqrt{gh}, \quad \lambda_2 = un_x + vn_y, \quad \lambda_3 = un_x + vn_y + \sqrt{gh}. \quad (7)$$

The eigenvalues of the flux Jacobian are all real and are distinct if the water depth is nonzero, so the shallow water system given by (1) and (5) is strictly hyperbolic. These SWEs are used in this paper, and in the equations of following sections \mathbf{U} , \mathbf{E} , \mathbf{G} , and \mathbf{S} refer to (5).

3. The numerical method

In this work, the governing equations (1) and (5) are discretized spatially on the Delaunay triangular meshes using a high-resolution finite volume Godunov-type approach, with the HLLC approximate Riemann solver [41] chosen to calculate the inviscid fluxes across volume interfaces. The MUSCL reconstruction technique [44] is adopted to achieve second-order accuracy in space, and the second-order accuracy in time is obtained by using two-stage TVD Runge–Kutta method. The sloping bottom model together with volume/free-surface relationships (VFRs) [8] is incorporated into the present scheme for wetting and drying.

3.1. Sloping bottom model

In this study, the flow variables are specified at the centroid of each cell, whereas the bed elevations are defined at the vertices of triangular grids to represent terrain with second-order spatial accuracy. The terrain within each cell is assumed to be varied linearly, so the bed elevation at both sides of a face is equal, and the bed elevation at the middle point of the interface is determined and unique. The conservative variable h denotes a cell-average of water depth, whereas the water level η is defined to be the free surface elevation in the wetted portion of the cell [8]. The gradients of bottom in cell C_i are:

$$\alpha_i = \frac{\partial b_i(x, y)}{\partial x} = \frac{1}{2\Omega_i} [(y_{i,2} - y_{i,3})b_{i,1} + (y_{i,3} - y_{i,1})b_{i,2} + (y_{i,1} - y_{i,2})b_{i,3}], \quad (8)$$

$$\beta_i = \frac{\partial b_i(x, y)}{\partial y} = \frac{1}{2\Omega_i} [(x_{i,3} - x_{i,2})b_{i,1} + (x_{i,1} - x_{i,3})b_{i,2} + (x_{i,2} - x_{i,1})b_{i,3}], \quad (9)$$

where Ω_i denotes the area of cell C_i ; $x_{i,k}$, $y_{i,k}$, and $b_{i,k}$ are x -, y -Cartesian coordinates and bed elevation at vertex v_k ($k = 1, 2, 3$) in cell C_i , supposing that the vertices $v_1 - v_2 - v_3$ is in the anti-clockwise direction.

Without loss of universality, in the following equations it will be assumed that $b_{i,1} \leq b_{i,2} \leq b_{i,3}$. Note that the cell average of water depth, h_i , is a conservative variable, and then the volume of water

in C_i is equal to $h_i\Omega_i$. To make a distinction between the water surface elevation of cell and the cell-averaged depth, the water level is computed by VFRs [8] provided that the water depth is given and the free surface elevation is uniform in partially submerged cells

$$\eta_i = \begin{cases} \eta_i^1 = b_{i,1} + \sqrt[3]{3h_i(b_{i,2} - b_{i,1})(b_{i,3} - b_{i,1})} & \text{if } b_{i,1} < \eta_i^1 \leq b_{i,2}, \\ \eta_i^2 = \frac{1}{2}(-\gamma_1 + \sqrt{\gamma_1^2 - 4\gamma_2}) & \text{if } b_{i,2} < \eta_i^2 \leq b_{i,3}, \\ \eta_i^3 = h_i + (b_{i,1} + b_{i,2} + b_{i,3})/3 & \text{if } \eta_i^3 > b_{i,3}, \end{cases} \quad (10)$$

where

$$\gamma_1 = b_{i,3} - 3b_{i,1}, \quad \gamma_2 = 3h_ib_{i,1} - 3h_ib_{i,3} - b_{i,2}b_{i,3} + b_{i,1}b_{i,2} + b_{i,1}^2. \quad (11)$$

There are three different situations in (10), and the correct case depends on the value of water level which is unknown before calculation. However, this problem can be easily resolved by the method of trial and error. By introducing the sloping bottom model and VFRs, the water surface elevation of cell can take on any elevation including elevations below the bed at the centroid. Further, cells can be classified as fully submerged, partially submerged and dry when $\eta_i > b_{i,3}$, $b_{i,1} < \eta_i \leq b_{i,3}$ and $\eta_i \leq b_{i,1}$, respectively. This is the one corresponding to the horizontal free surface classification method proposed by Begnudelli and Sanders [6]. The free surface elevation is assumed to be uniform in partially submerged cells. Bradford and Sanders [11] and Begnudelli and Sanders [8,6] used another method that classifies a cell as wet if and only if all nodes are wet. However, a dry cell might have three wet nodes, and then would be classified as wet. To resolve this problem, a cell should be classified as wet when the volume of water is enough to submerge the highest node based on the assumption of a horizontal water surface. The horizontal free surface classification method may be of benefit to model stability since the momentum equations are not solved in the partially submerged cells.

Let superscript n denote the time step level. If $\eta_i^n > b_{i,3}$ and $\eta_i^{n+1} > b_{i,3}$, then from (10) we can conclude that $\eta_i^{n+1} - \eta_i^n = h_i^{n+1} - h_i^n$, so the mass conservation can be exactly preserved if η is used to update solutions, i.e. (1) and (4) can preserve mass conservation under the condition of fully submerged cell. However, the inequality $\eta_i^{n+1} - \eta_i^n \neq h_i^{n+1} - h_i^n$ is true when the cell is partially submerged, thus the use of η to update the solutions can not exactly preserve the mass conservation. A hypothetical numerical example is given as follows to reveal this mass error.

In the case of the i th triangular cell, suppose that the bottom elevations of three vertices are $b_{i,1} = 1$ m, $b_{i,2} = 10$ m, $b_{i,3} = 20$ m, and the cell is dry at the time step level n , i.e. $h_i^n = 0$, $\eta_i^n = 1$ m. Assume that the computed value $F_i^{\text{mass}} = (-\Delta t \sum_{k=1}^3 \mathbf{F}_{i,k}^{(0)} \cdot \mathbf{n}_{i,k} L_{i,k} / \Omega_i)^n$ is 15 m (see Sections 3.2 and 3.7 for details of the finite volume method and the time stepping scheme, where $\mathbf{F}^{(0)}$ denotes the first component of the numerical flux \mathbf{F}). If the water level η is used to update the solution, then $\eta_i^{n+1} = \eta_i^n + F_i^{\text{mass}} = 16$ m. From the inverse formulation of (10) [8], we can compute that $h_i^{n+1} = 5.95$ m. So the mass error from using η to update the solution is $15\Omega_i - 5.95\Omega_i = 9.05\Omega_i \text{ m}^3$. On the other hand, if we use h to update the solution, then $h_i^{n+1} = h_i^n + F_i^{\text{mass}} = 15$ m, and the mass is conserved. Furthermore, from (10) we can compute that $\eta_i^{n+1} = 25.3$ m.

It should be noted that the mass error from using η to update the solutions in a partially submerged cell is irrelevant to the numerical flux, but is associated with the bottom slope of the cell. The mass error may not be important in cases with more or less uniform bed, but as the bed undulations increase and relatively coarse grids are used, this error may be too significant to be

ignored in the process of wetting and drying. In this situation, the water depth should be used to update the solutions just as the SWEs given by (1) and (5).

It should be noted that, when the bed elevation is defined at the centroid of each cell and the terrain within each cell is assumed to be flat, cells are only classified as fully submerged and dry (whereas no partially submerged cell exists), so $\eta_i^{n+1} - \eta_i^n = h_i^{n+1} - h_i^n$ is true and the mass conservation can be exactly preserved by using water level η as a basis variable to update the solution, i.e. (1) and (4) can exactly preserve the mass conservation under this condition of bed elevation definition. For example, the use of water level η , mathematically or numerically, as a flow variable has been well-established in literatures [30,31] to achieve conservative and well-balanced schemes.

3.2. Finite volume method

The integral form of (1) is

$$\frac{\partial}{\partial t} \int_{\Omega} \mathbf{U} d\Omega + \int_{\Omega} \left(\frac{\partial \mathbf{E}}{\partial x} + \frac{\partial \mathbf{G}}{\partial y} \right) d\Omega = \int_{\Omega} \mathbf{S} d\Omega. \quad (12)$$

Applying Green's theorem, (12) becomes

$$\frac{\partial}{\partial t} \int_{\Omega} \mathbf{U} d\Omega + \oint_{\partial\Omega} \mathbf{F} \cdot \mathbf{n} dl = \int_{\Omega} \mathbf{S} d\Omega \quad (13)$$

in which Ω is the control volume; $\partial\Omega$ denotes the boundary of the volume; \mathbf{n} is the unit outward vector normal to the boundary; $d\Omega$ and dl are the area and arc elements, respectively. The integrand $\mathbf{F} \cdot \mathbf{n}$ is the outward normal flux vector in which $\mathbf{F} = [\mathbf{E}, \mathbf{G}]^T$. In a 2D triangular grid system, the line integral term in (13) is evaluated as

$$\oint_{\partial\Omega} \mathbf{F} \cdot \mathbf{n} dl = \sum_{k=1}^3 \mathbf{F}_k(\mathbf{U}_L, \mathbf{U}_R) \cdot \mathbf{n}_k L_k, \quad (14)$$

where the subscript k denotes the index of edge of triangular cell; L is the arc length; \mathbf{U}_L and \mathbf{U}_R are the left and right states for a local Riemann problem, respectively. Consider the rotation matrix and its inverse matrix

$$\mathbf{T}_n = \begin{bmatrix} 1 & 0 & 0 \\ 0 & n_x & n_y \\ 0 & -n_y & n_x \end{bmatrix}, \quad \mathbf{T}_n^{-1} = \begin{bmatrix} 1 & 0 & 0 \\ 0 & n_x & -n_y \\ 0 & n_y & n_x \end{bmatrix}, \quad (15)$$

where $\mathbf{n} = (n_x, n_y)^T$. By using the rotational invariance property of the SWEs [41], we have

$$\mathbf{F}_k(\mathbf{U}_L, \mathbf{U}_R) \cdot \mathbf{n}_k = \mathbf{T}_n^{-1} \mathbf{E}(\mathbf{T}_n \mathbf{U}_L, \mathbf{T}_n \mathbf{U}_R). \quad (16)$$

Let

$$\hat{\mathbf{U}} = \mathbf{T}_n \mathbf{U} = \begin{bmatrix} h \\ h(un_x + vn_y) \\ h(-un_y + vn_x) \end{bmatrix} = \begin{bmatrix} h \\ hu_{\perp} \\ hu_{//} \end{bmatrix}, \quad (17)$$

where $u_{\perp} = un_x + vn_y$ and $u_{//} = -un_y + vn_x$ are the velocity perpendicular and tangential to the cell face, respectively. Then

$$\mathbf{F}(\mathbf{U}) \cdot \mathbf{n} = \mathbf{T}_n^{-1} \mathbf{E}(\hat{\mathbf{U}}) = \begin{bmatrix} hu_{\perp} \\ huu_{\perp} + \frac{1}{2}g(h^2 - b^2)n_x \\ hvu_{\perp} + \frac{1}{2}g(h^2 - b^2)n_y \end{bmatrix}. \quad (18)$$

Eq. (16) means that the two-dimensional SWEs can be solved by transforming \mathbf{U} into $\hat{\mathbf{U}}$ and solving the corresponding local one-dimensional Riemann problems.

The finite volume method is based on (13) and (14), and the discretization of (13) ensures that the mass and momentum will be conserved across a discontinuity [28]. Discretizing (13) in an arbitrary triangular cell C_i , the equation becomes

$$\Omega_i \frac{d\mathbf{U}_i}{dt} = - \sum_{k=1}^3 \mathbf{F}_{i,k}(\mathbf{U}_L, \mathbf{U}_R) \cdot \mathbf{n}_{i,k} L_{i,k} + \mathbf{S}_i, \quad (19)$$

where $\mathbf{U}_i = 1/\Omega_i \int_{C_i} \mathbf{U} d\Omega$ is the cell-averaged conserved vector, Ω_i is the area of cell C_i ; i and k are the cell index and edge index, respectively; \mathbf{S}_i is the source approximation associated with cell C_i .

3.3. HLLC approximate Riemann solver

Many approximate Riemann solvers have been proposed which can be applied more efficiently than the exact Riemann solver while yet achieving equally good results in many cases. Recent advances are outlined in the books by Toro [41] and LeVeque [28]. The HLLC approximate Riemann solver [41] is adopted in this study because it is entropy satisfying and is suited to cases involving wetting and drying provided that the wave speed is chosen appropriately [52]. The interface flux of HLLC is computed as follows

$$\mathbf{F}(\mathbf{U}_L, \mathbf{U}_R) \cdot \mathbf{n} = \begin{cases} \mathbf{F}_L & \text{if } s_1 \geq 0, \\ \mathbf{F}_{*L} & \text{if } s_1 < 0 \leq s_2, \\ \mathbf{F}_{*R} & \text{if } s_2 < 0 < s_3, \\ \mathbf{F}_R & \text{if } s_3 \leq 0, \end{cases} \quad (20)$$

where $\mathbf{F}_L = \mathbf{F}(\mathbf{U}_L) \cdot \mathbf{n}$ and $\mathbf{F}_R = \mathbf{F}(\mathbf{U}_R) \cdot \mathbf{n}$ are both computed by (18). \mathbf{U}_L and \mathbf{U}_R are the left and right Riemann states for a local Riemann problem, respectively. In fully submerged cells, the face values are obtained from the cell central values of the flow variables using a limited piece-wise linear reconstruction to achieve a high-resolution and second-order spatially accurate finite volume scheme. \mathbf{F}_{*L} and \mathbf{F}_{*R} are the numerical fluxes in the left and right sides of the middle region of the Riemann solution which is divided by a contact wave; and s_1, s_2, s_3 are estimates of the speeds of the left, contact and right waves, respectively. The middle wave arising from the presence of the tangential momentum equation is always a shear wave, across which the tangential velocity component changes discontinuously whereas perpendicular velocity component and water depth remain constant. Either side of the middle wave, the middle region fluxes \mathbf{F}_{*L} and \mathbf{F}_{*R} are different, and are given by

$$\mathbf{F}_{*L} = \begin{bmatrix} (\mathbf{E}_{HLL})^1 \\ (\mathbf{E}_{HLL})^2 n_x - u_{//L} (\mathbf{E}_{HLL})^1 n_y \\ (\mathbf{E}_{HLL})^2 n_y + u_{//L} (\mathbf{E}_{HLL})^1 n_x \end{bmatrix}, \quad \mathbf{F}_{*R} = \begin{bmatrix} (\mathbf{E}_{HLL})^1 \\ (\mathbf{E}_{HLL})^2 n_x - u_{//R} (\mathbf{E}_{HLL})^1 n_y \\ (\mathbf{E}_{HLL})^2 n_y + u_{//R} (\mathbf{E}_{HLL})^1 n_x \end{bmatrix}, \quad (21)$$

where $u_{//L}$ and $u_{//R}$ are the left and right initial velocity tangential to the interface of a local Riemann problem, which remain unchanged across the left and right waves, respectively. $(\mathbf{E}_{HLL})^1$ and $(\mathbf{E}_{HLL})^2$ are the first two components of the normal flux \mathbf{E}_{HLL} which is calculated using the HLL formula proposed by Harten et al. [24]

$$\mathbf{E}_{HLL} = \frac{s_3 \mathbf{E}(\hat{\mathbf{U}}_L) - s_1 \mathbf{E}(\hat{\mathbf{U}}_R) + s_1 s_3 (\hat{\mathbf{U}}_R - \hat{\mathbf{U}}_L)}{s_3 - s_1}, \quad (22)$$

From (20) and (22) we know that, wave speeds have significant effect on the numerical fluxes, and the appropriate method for wave speeds approximation is the key to the success of HLLC solver. Different choices of wave speed estimates for SWEs are possible. Fraccarollo and Toro [19] and Liang and Borthwick [29] recommend the use of two rarefactions assumption and dry-bed options for the left and right wave speeds. Zia and Banihashemi [52] adopted the approximations including shock, rarefaction and dry bed options. In this paper, the two rarefactions assumption and dry-bed options for the left and right wave speeds are used, whereas the middle

state approximations are replaced by Roe average. This is referred as the Einfeldt speeds [23] given by

$$s_1 = \begin{cases} \min(u_{\perp,L} - \sqrt{gh_L}, u_{\perp,*} - \sqrt{gh_*}) & \text{if } h_L > 0, \\ u_{\perp,R} - 2\sqrt{gh_R} & \text{if } h_L = 0, \end{cases} \quad s_3 = \begin{cases} \max(u_{\perp,R} + \sqrt{gh_R}, u_{\perp,*} + \sqrt{gh_*}) & \text{if } h_R > 0, \\ u_{\perp,L} + 2\sqrt{gh_L} & \text{if } h_R = 0, \end{cases} \quad (23)$$

where $u_{\perp,L}, u_{\perp,R}, h_L$ and h_R are the components of left and right initial Riemann states for a local Riemann problem, and h_* and $u_{\perp,*}$ are the Roe averaged quantities

$$h_* = \frac{1}{2}(h_L + h_R) \quad u_{\perp,*} = \frac{\sqrt{h_L} u_{\perp,L} + \sqrt{h_R} u_{\perp,R}}{\sqrt{h_L} + \sqrt{h_R}}. \quad (24)$$

The Einfeldt speed in practice gives sharp result for shock waves, since the shock speed is smaller than the characteristic speed behind the shock and in this situation the Einfeldt speed reduces to the Roe approximation of the shock speed [28]. According to Toro's suggestion [41], the middle wave speed is calculated from

$$s_2 = \frac{s_1 h_R (u_{\perp,R} - s_3) - s_3 h_L (u_{\perp,L} - s_1)}{h_R (u_{\perp,R} - s_3) - h_L (u_{\perp,L} - s_1)}. \quad (25)$$

3.4. Variable reconstruction and slope limiter

If the variables are approximated as constant within each cell and then the fluxes at interfaces are estimated by solving Riemann problems that employ the values of variables in either sides of the face as the initial discontinuity condition, the corresponding scheme is only first-order spatial accuracy, and gives excessive numerical dissipation. To achieve higher-order accuracy, better reconstruction techniques than a piecewise constant function always be used (see e.g. [51,25,6,3,5,16]).

In this study, if a cell is identified as partially submerged, face values of the velocities are extrapolated from centroid values:

$$u_{i,k}^{\text{Rec}} = u_i \quad v_{i,k}^{\text{Rec}} = v_i \quad (k = 1, 2, 3). \quad (26)$$

Generally, reconstruction of the water depth on the cell face is obtained by subtracting bed elevation at the face midpoint from reconstructed value of the water surface elevation, and when the reconstructed water depth is computed to be a negative number, it is set to zero [8]. However, this leads to a drawback of trapping small water volumes on sloping beds if the direction of steepest descent is not aligned with the grid [6]. To relieve this problem, the method for water depth reconstruction proposed by Begnudelli and Sanders [6] is used in this study:

$$h_{i,k}^{\text{Rec}} = \begin{cases} 0 & \text{if } \eta_i \leq b_{i,k}^{\min} \\ \frac{(\eta_i - b_{i,k}^{\min})^2}{2(b_{i,k}^{\max} - b_{i,k}^{\min})} & \text{if } b_{i,k}^{\min} < \eta_i \leq b_{i,k}^{\max} \\ \eta_i - \frac{b_{i,k}^{\min} + b_{i,k}^{\max}}{2} & \text{if } \eta_i > b_{i,k}^{\max} \end{cases} \quad (k = 1, 2, 3), \quad (27)$$

where η_i is the water surface elevation of cell C_i and is computed from (10); $b_{i,k}^{\min}$ and $b_{i,k}^{\max}$ are the minimum and maximum bed elevations of the two endpoints of edge k in cell C_i . See Section 3.7 for wet/dry fronts sharpening to further resolve this problem. Eqs. (26) and (27) indicate that the scheme reverts to the first-order spatial accuracy in partially submerged cells.

If a cell is identified as fully submerged, face values, such as η , hu , and hv , are calculated using limited linear interpolation

$$p(x, y) = p_i + \nabla p_i \cdot \mathbf{r} \quad (28)$$

where p is any of the variables to be reconstructed; (x, y) is the point where the interpolation are required, i.e. the midpoint of the cell faces; \mathbf{r} is the position vector of point (x, y) relative to the cell centre; ∇p_i is the limited gradient, which is given by

$$\nabla p_i = \varphi_i \nabla p_i, \quad (29)$$

where φ_i is the limit function; ∇p_i is the unlimited gradient. The unlimited gradient of a generic dependent variable p is based on its values p_1 , p_2 , and p_3 at three neighboring cell centroid, (x_1, y_1) , (x_2, y_2) , and (x_3, y_3) , which are numbered in the counter-clockwise direction, respectively. The unlimited gradient of p is given by

$$\nabla p = (-\mu^2/\mu^3, -\mu^1/\mu^3) \quad (30)$$

in which $\boldsymbol{\mu} = (\mu^1, \mu^2, \mu^3) = (\mathbf{P}_1 - \mathbf{P}_3) \times (\mathbf{P}_2 - \mathbf{P}_3)$; $\mathbf{P}_k = (x_k, y_k, p_k)^T$ ($k = 1, 2, 3$).

The limit function is given by [25]

$$\varphi_i = \min_{k=1,2,3}(\varphi_k), \quad \varphi_k = \begin{cases} \min \left[1, \frac{\max(0, p_{i,k}^{\text{nc}} - p_i)}{p_{i,k}^{\text{rec}} - p_i} \right] & \text{if } p_{i,k}^{\text{rec}} - p_i > 0, \\ \min \left[1, \frac{\min(0, p_{i,k}^{\text{nc}} - p_i)}{p_{i,k}^{\text{rec}} - p_i} \right] & \text{if } p_{i,k}^{\text{rec}} - p_i < 0, \\ 1 & \text{if } p_{i,k}^{\text{rec}} - p_i = 0, \end{cases} \quad (31)$$

where $p_{i,k}^{\text{rec}} = p_i + \nabla p_i \cdot \mathbf{r}_{i,k}$ represents the unlimited reconstructed value of p at the midpoint of the k th face of the i th cell, and $p_{i,k}^{\text{nc}}$ is the value of p at the centroid of the k th adjacent cell which shares the k th face of the i th cell. After the limited gradients of water surface are computed, water depths at the three vertices of a cell are obtained by a limited reconstruction of the water surface elevation η at the cell vertices and subtracting the corresponding vertex bottom elevations. If there is at least one vertex that has a negative reconstructed value of water depth, then all gradients of this cell are set to zero and the face values of primitive variables are extrapolated from centroid values. Otherwise, reconstructed value of water depth h is obtained by subtracting bottom elevation at the face midpoint from reconstructed value of the water surface elevation. The reconstructed velocities are calculated by

$$\mathbf{u}^{\text{rec}} = (hu)^{\text{rec}}/h^{\text{rec}}, \quad \mathbf{v}^{\text{rec}} = (hv)^{\text{rec}}/h^{\text{rec}}. \quad (32)$$

Eq. (32) might introduce unphysical large velocities even for sub-critical flow, and further lead to numerical instability. To deal with this problem, all gradients of flow variables are set to zero when the reconstructed velocity is bigger than a critical value (30 m/s is used in this study, and other solution-adaptive values can be adopted), and then the reconstructed face values of the flow variables are extrapolated from centroid values. Simply using the critical value can essentially avoid the reconstruction of large velocity, and sometimes leads to a similar behavior of the adaptive method [5], which is worth further investigation.

3.5. Bed slopes treatments

Source terms can be split into bed slopes and friction terms as indicated in (5). In this paper, the bed slope term $\mathbf{S}_{i,0} = (0, S_{i,0x}, S_{i,0y})^T$ is directly approximated as follows without regard for cell's wet/dry status

$$S_{i,0x} = - \int_{C_i} g(h+b)\alpha_i d\Omega = -g(h_i+b_i)\alpha_i \Omega_i, \quad (33)$$

$$S_{i,0y} = - \int_{C_i} g(h+b)\beta_i d\Omega = -g(h_i+b_i)\beta_i \Omega_i. \quad (34)$$

To provide a well-balanced scheme for shallow flows with wetting and drying, Liang and Marche [30] proposed the additional terms for bed slope term approximation; Begnudelli and Sanders

[8] introduced the flux correction terms. However, the model proposed in this paper doesn't need any special treatment to preserve well-balanced property. This is demonstrated as follows.

Considering a stationary flow case of $\eta = \text{Constant}$, $u = v = 0$. The all mass fluxes are computed to be zero since the water depths at both sides of each face are equal and the velocities are zero. When a cell is fully submerged, the outward normal fluxes across three faces are:

$$\sum_{k=1}^3 \mathbf{F}_{i,k} \cdot \mathbf{n}_{i,k} L_{i,k} = \begin{bmatrix} 0 \\ \sum_{k=1}^3 \frac{1}{2} g(h_{i,k}^2 - z_{i,k}^2) L_{i,k} n_{i,k}^x \\ \sum_{k=1}^3 \frac{1}{2} g(h_{i,k}^2 - z_{i,k}^2) L_{i,k} n_{i,k}^y \end{bmatrix}, \quad (35)$$

where the subscripts i and k denote the cell number and face number, respectively; $\mathbf{n}_{i,k} = (n_{i,k}^x, n_{i,k}^y)^T$; h and z are the reconstructed water depth and bed elevation at the midpoint of face. Because the cell is fully submerged, so $h_{i,k} = \eta - z_{i,k}$ ($k = 1, 2, 3$), and

$$\begin{aligned} \sum_{k=1}^3 \mathbf{F}_{i,k} \cdot \mathbf{n}_{i,k} L_{i,k} &= \begin{bmatrix} 0 \\ \sum_{k=1}^3 \frac{1}{2} g(\eta^2 - 2\eta z_{i,k}) L_{i,k} n_{i,k}^x \\ \sum_{k=1}^3 \frac{1}{2} g(\eta^2 - 2\eta z_{i,k}) L_{i,k} n_{i,k}^y \end{bmatrix} \\ &= \frac{1}{2} g \eta^2 \begin{bmatrix} 0 \\ \sum_{k=1}^3 L_{i,k} n_{i,k}^x \\ \sum_{k=1}^3 L_{i,k} n_{i,k}^y \end{bmatrix} - g \eta \begin{bmatrix} 0 \\ \sum_{k=1}^3 z_{i,k} L_{i,k} n_{i,k}^x \\ \sum_{k=1}^3 z_{i,k} L_{i,k} n_{i,k}^y \end{bmatrix}. \end{aligned} \quad (36)$$

Let x_{ij} , y_{ij} , and b_{ij} denote, respectively, the x -, y -Cartesian coordinates and bed elevation at vertex v_j ($j = 1, 2, 3$) in cell C_i , and suppose that the vertices $v_1 - v_2 - v_3$ is in the anti-clockwise direction and the edge is numbered by the opposite vertex number. Then $L_{i,1} n_{i,1}^x = y_{i,3} - y_{i,2}$, $L_{i,2} n_{i,2}^x = y_{i,1} - y_{i,3}$, $L_{i,3} n_{i,3}^x = y_{i,2} - y_{i,1}$, $L_{i,1} n_{i,1}^y = x_{i,2} - x_{i,3}$, $L_{i,2} n_{i,2}^y = x_{i,3} - x_{i,1}$, $L_{i,3} n_{i,3}^y = x_{i,1} - x_{i,2}$, $z_{i,1} = (b_{i,2} + b_{i,3})/2$, $z_{i,2} = (b_{i,1} + b_{i,3})/2$, $z_{i,3} = (b_{i,1} + b_{i,2})/2$. Thus

$$\sum_{k=1}^3 L_{i,k} n_{i,k}^x = 0, \quad \sum_{k=1}^3 L_{i,k} n_{i,k}^y = 0 \quad (37)$$

and

$$\sum_{k=1}^3 z_{i,k} L_{i,k} n_{i,k}^x = \alpha_i \Omega_i, \quad \sum_{k=1}^3 z_{i,k} L_{i,k} n_{i,k}^y = \beta_i \Omega_i. \quad (38)$$

So

$$\sum_{k=1}^3 \mathbf{F}_{i,k} \cdot \mathbf{n}_{i,k} L_{i,k} = \begin{bmatrix} 0 \\ -g\eta\alpha_i\Omega_i \\ -g\eta\beta_i\Omega_i \end{bmatrix}. \quad (39)$$

Besides, the friction terms can't influence the solutions since the velocity is zero. So from (19) we have

$$\Omega_i \frac{d\mathbf{U}_i}{dt} = - \sum_{k=1}^3 \mathbf{F}_{i,k}(\mathbf{U}_L, \mathbf{U}_R) \cdot \mathbf{n}_{i,k} L_{i,k} + \mathbf{S}_i = \mathbf{0}. \quad (40)$$

Eq. (40) means that the stationary solutions are exactly preserved in fully submerged cell. See Section 3.7 for the treatment of partially submerged cell that retains a zero velocity. So the present model is well-balanced and preserves the exact C-property [9].

3.6. Friction terms treatments

Generally, the friction component of the source terms is solved by a splitting method [28,39]. Song et al. [39] demonstrated the

potential stiff problem due to two-stage explicit TVD Runge–Kutta treatment of the friction term, and concluded that the stiff problem can significant effect on the stability and efficiency of the numerical scheme. To deal with this problem, implicit scheme [30,48] and semi-implicit [8,39] scheme are widely used. Liang and Marche [30] introduced a limiting value of the implicit friction force to ensure that the maximum effect of friction force is to stop the fluid, which indicates that the direction of velocity components can not be inverted by friction terms.

In this paper, the friction terms are solved by the semi-implicit scheme [8,39] which is given by

$$u^{n+1} = \frac{1}{1 + \Delta t \hat{\tau}^n} \hat{u}^n, \quad v^{n+1} = \frac{1}{1 + \Delta t \hat{\tau}^n} \hat{v}^n, \quad (41)$$

where $\hat{\tau}^n = gn^2 \sqrt{(\hat{u}^n)^2 + (\hat{v}^n)^2} (\hat{h}^n)^{-4/3}$; \hat{h}^n , \hat{u}^n , and \hat{v}^n are the initial states for the friction source term treatment. This scheme doesn't invert the direction of velocity components, i.e. $u^{n+1} \cdot \hat{u}^n \geq 0$, and $v^{n+1} \cdot \hat{v}^n \geq 0$, thus enhances the model stability. Moreover, (41) may relieve the problem of high velocity with small water depth in friction case. For example, let $\hat{h}^n = 10^{-2}$ m, $\hat{u}^n = 800$ m/s, $\hat{v}^n = -900$ m/s, $n = 0.018$ s/m^{1/3}, $\Delta t = 0.1$ s, then the velocities computed by (41) are $\hat{u}^n = 4.48$ m/s and $\hat{v}^n = -5.04$ m/s. This indicates that the friction terms could even benefit computational stability when the semi-implicit scheme (41) is used.

3.7. Time stepping

In the framework of Godunov-type finite volume scheme, the following time-marching formula may be used to update the flow variables to the next time step:

$$\mathbf{U}_i^{n+1} = \mathbf{U}_i^n - \frac{\Delta t}{\Omega_i} \left(\sum_{k=1}^3 \mathbf{F}_{i,k}(\mathbf{U}_L, \mathbf{U}_R) \cdot \mathbf{n}_{i,k} L_{i,k} - \mathbf{S}_i \right), \quad (42)$$

where the superscript n is the time level, Δt is the time step. A Godunov-type scheme is first-order accurate in time if the flow variables are updated using the time-marching formula (42), which gives excessive diffusive results. In this study, the two-stage explicit TVD Runge–Kutta method is employed to achieve second-order accuracy in time. Accordingly, the time discretization formula of (19) may be written as:

$$\mathbf{U}_i^{n+1} = \frac{1}{2} (\mathbf{U}_i^n + \mathbf{U}_i^{(2)}), \quad (43)$$

where

$$\mathbf{U}_i^{(2)} = \mathbf{U}_i^{(1)} + \Delta t \mathbf{L}_i(\mathbf{U}^{(1)}), \quad \mathbf{U}_i^{(1)} = \mathbf{U}_i^n + \Delta t \mathbf{L}_i(\mathbf{U}^n), \quad (44)$$

where \mathbf{L}_i is defined by

$$\mathbf{L}_i(\mathbf{U}) = -\frac{1}{\Omega_i} \left(\sum_{k=1}^3 \mathbf{F}_{i,k} \cdot \mathbf{n}_{i,k} L_{i,k} - \mathbf{S}_{i,0} \right) + \tilde{\mathbf{S}}_{if}, \quad (45)$$

where $\mathbf{S}_{i,0}$ is the bed slope source term estimation of C_i and its components are computed by (33) and (34); $\tilde{\mathbf{S}}_{if}$ denotes the influence of friction term. In summary, the process of time stepping is:

Step1: Compute the fluxes and bed slope estimate, and then \mathbf{U}^n is updated by:

$$\hat{\mathbf{U}}_i^{(1)} = \mathbf{U}_i^n - \frac{\Delta t}{\Omega_i} \left(\sum_{k=1}^3 \mathbf{F}_{i,k} \cdot \mathbf{n}_{i,k} L_{i,k} - \mathbf{S}_{i,0} \right). \quad (46)$$

Step2: Make the result of (46) $\hat{\mathbf{U}}_i^{(1)}$ be the initial value, then the velocity components of $\mathbf{U}_i^{(1)}$ are computed by (41), and the water depth component of $\mathbf{U}_i^{(1)}$ is the same as that of $\hat{\mathbf{U}}_i^{(1)}$.

Step3: Sharpen the wet/dry fronts of $\mathbf{U}^{(1)}$. Cells are classified as four types: (1) fully submerged, (2) dry, (3) partially submerged with a submerged neighbor whose water surface elevation is bigger than the lowest nodal bed elevation of this cell (the cell to be classified), and (4) otherwise. The total water volume of the fourth-type cells is averagely distributed to the third-type cells. Subsequently, the water depths and velocities in the fourth-type cells are set to be zero. According to Bradford and Sanders [11], the velocities in the third-type cells are extrapolated from the neighboring submerged cell with the largest water depth. It should be noted that negative water depths could be predicted at this time, then the computed water depths lower than zero are set at zero, and the corresponding velocities are also set at zero.

Step4: Repeat step1, step2, and step 3 by employing $\mathbf{U}^{(1)}$ as the initial state to get $\mathbf{U}^{(2)}$, and the solution is updated by (43). Finally, step 3 is used again to sharpen the wet/dry fronts of \mathbf{U}^{n+1} .

3.8. Boundary conditions

Boundary conditions are implemented by means of fluxes computation at boundaries. According to (18), the normal flux at the boundary is given as

$$\mathbf{F} \cdot \mathbf{n} = \begin{bmatrix} h_* u_{\perp,*} \\ h_* u_{\perp,*} + \frac{1}{2} g (h_*^2 - b^2) n_x \\ h_* v_* u_{\perp,*} + \frac{1}{2} g (h_*^2 - b^2) n_y \end{bmatrix}, \quad (47)$$

where the subscript $*$ denotes variables at the boundary, which is restricted by using Riemann invariants of one-dimensional SWEs based on characteristic theory as follows [48]

$$u_{\perp,*} + 2\sqrt{gh_*} = u_{\perp,L} + 2\sqrt{gh_L}, \quad (48)$$

where the subscript L denotes the variables at the side of inner cell, and also at the left side of the boundary. To compute the variables at boundaries, boundary conditions are needed to construct another equality constraint.

In the case of a depth boundary condition, h_* is given and $u_{\perp,*}$ is computed directly from (48) as

$$u_{\perp,*} = u_{\perp,L} + 2\sqrt{gh_L} - 2\sqrt{gh_*}. \quad (49)$$

In the case of a velocity boundary condition, $u_{\perp,*}$ is given and h_* is computed by transforming (48) as

$$h_* = [u_{\perp,L} + 2\sqrt{gh_L} - u_{\perp,*}]^2 / 4g. \quad (50)$$

In the case of an inflow boundary condition, $q_{\perp,*}$ is given as

$$q_{\perp,*} = h_* u_{\perp,*}, \quad (51)$$

where $q_{\perp,*}$ denotes unit discharge and $q_{\perp,*} < 0$. h_* and $u_{\perp,*}$ are computed by substituting of $q_{\perp,*}/h_* = u_{\perp,*}$ into (48):

$$f(c_*) = c_*^3 - \frac{a_L}{2} c_*^2 + \frac{1}{2} g q_{\perp,*} = 0, \quad (52)$$

where $c_* = \sqrt{gh_*} \geq 0$, $a_L = u_{\perp,L} + 2\sqrt{gh_L}$. The root of (52) always exists and is unique since $q_{\perp,*} < 0$. In this paper, the Newton–Raphson iterative method is adopted to search the root, and we select a small positive value as the initial point of the Newton–Raphson iterative procedure when $a_L < 0$, and select a value little more than $a_L/3$ when $a_L > 0$.

Assume that the tangential velocity at a boundary is equal to that of left side, i.e.

$$u_{//,*} = u_{//,L}. \tag{53}$$

Then u_* and v_* can be computed as

$$u_* = u_{\perp,*}n_x - u_{//,*}n_y, \quad v_* = u_{\perp,*}n_y + u_{//,*}n_x. \tag{54}$$

Finally, the normal fluxes at boundaries can be computed by (47) based on h_* , u_* and v_* .

In the case of a solid slip boundary, i.e., the normal velocity component at the boundary $u_{\perp,*}$ is zero, so the normal flux is computed by (47) provided that the water depth at the boundary h_* is computed by (50) [48]. However, this method of calculation of h_* would introduce an erroneous great momentum flux and further produce an unphysical high velocity when the depth h_L is very small and $u_{\perp,L}$ is relatively big. To deal with this problem, a method simply using $h_* = h_L$ is adopted in this paper, which is also used by Liang and Borthwick [29].

In the case of a free outflow boundary, values of all variables at the boundary are equal to those of left side, and then the normal flux can be computed by (47).

3.9. Stability criteria

The numerical model is explicit, and its stability is controlled by the Courant-Friedrichs-Lewy (CFL) condition. For triangular grid system, the CFL condition for computing an appropriate time step used by time stepping procedure may be expressed

$$\Delta t = C_r \cdot \min_{i,k} \left[\left(\frac{\Omega}{(|u_{\perp}| + \sqrt{gh})_k L_k} \right)_i \right] \quad i = 1, 2, \dots, N; \quad k = 1, 2, 3, \tag{55}$$

where Δt is the time step; C_r is the Courant number specified in the range $0 < C_r \leq 1$, and $C_r = 0.8$ is adopted in this study; u_{\perp} and h are the Roe's average [28] of the reconstructed value at faces; N is the total number of cells. In the present model, an adaptive time step is used based on (55). The overall time step at each step is constrained by the largest $(|u_{\perp}| + \sqrt{gh})L/\Omega$ in the grid which may result from locally large $|u_{\perp}| + \sqrt{gh}$, small Ω/L , or both. It should be noted that the local time stepping method [27,37] can be implemented to achieve higher computational efficiency and is worth further integration into the present model.

4. Numerical results and discussion

In this section several benchmark problems are undertaken to test the performance of the proposed model. The unstructured meshes used in Section 4.1,4.2,4.3,4.4,4.5,4.6 result from a structured uniform meshes by dividing each orthogonal cell into four equal triangles. The length of the square grid is denoted by ξ to be specified in each case. All computational meshes are generated by using Triangle [38].

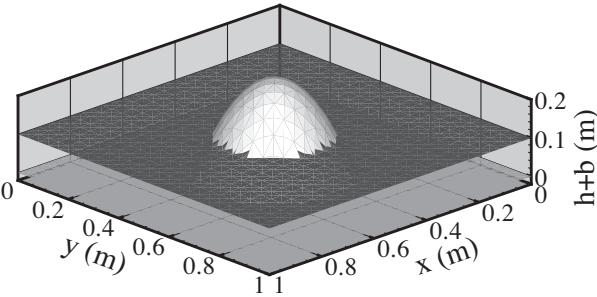


Fig. 2. Still water over a bump: The 3D water surface after $t = 500$ s and the bottom.

To validate the mass conservation of the present model, the following formula is used for quantifying mass error [37]:

$$\varepsilon = \max_t \left(\frac{|V_t - V_0 + \delta V_t|}{V_0} \right), \tag{56}$$

where ε represents the maximum relative error in global mass conservation over the simulation duration; V_0 is the initial volume of water and V_t is the computed volume of water at the time t ; δV_t

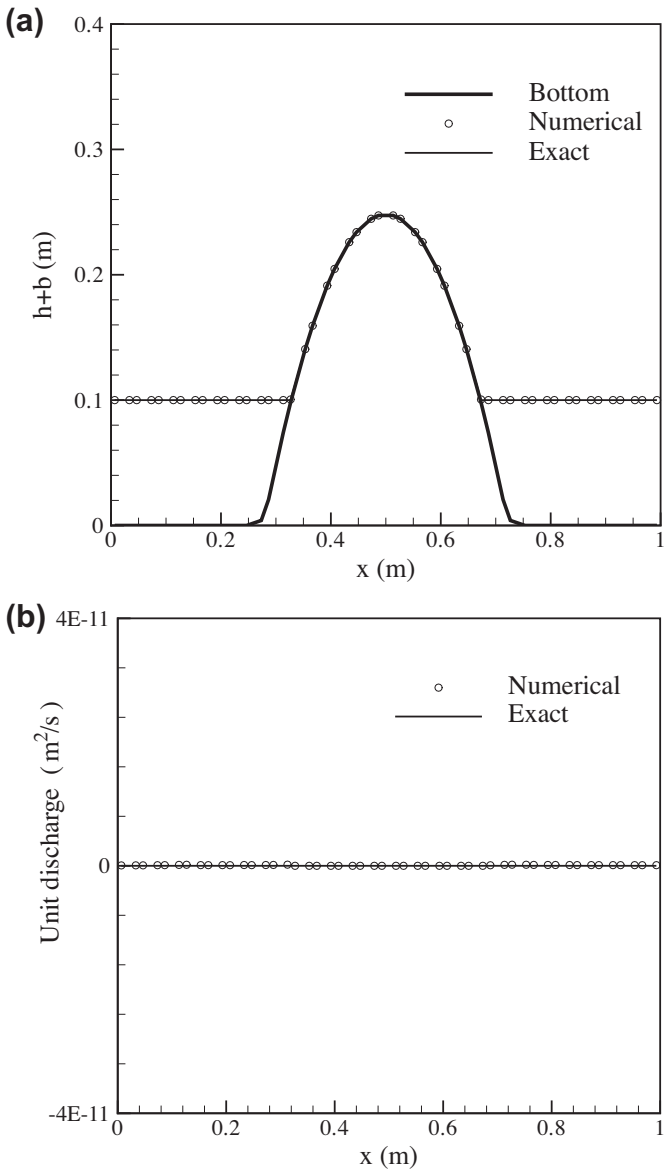


Fig. 3. Still water over a bump: (a) the water surface elevation and the bottom in cells along the line $y = 0.5$ m; (b) the corresponding unit discharge. The results are obtained at $t = 500$ s.

Table 1

Steady flow over a bump: initial and boundary conditions ($v = 0$ in all cases).

Cases	Initial conditions	Upstream boundary condition	Downstream boundary condition
2a	$\eta = 2.0$ m; $hu = 4.42$ m ² /s	$hu = 4.42$ m ² /s	$h = 2.0$ m
2b	$h = 0.33$ m; $hu = 0.18$ m ² /s	$hu = 0.18$ m ² /s	$h = 0.33$ m
2c	$h = 0.66$ m; $hu = 1.53$ m ² /s	$hu = 1.53$ m ² /s	Transmissive or $h = 0.66$ m

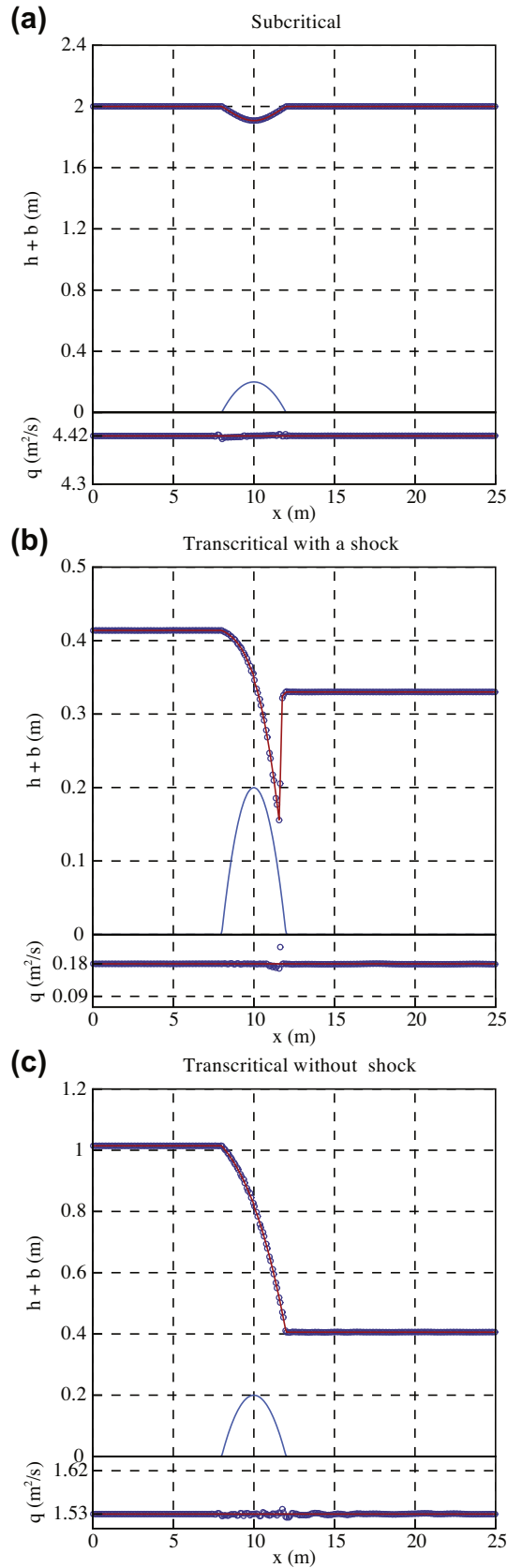


Fig. 4. Steady flow over a bump under different conditions: the water surface elevation and unit discharge in cells along the centerline of the channel. Exact solution and bottom elevation are given by solid lines; simulated results are given by circle.

represents the net volume transported out of the domain from the beginning of the simulation period to the time t .

4.1. Preservation of still water over a two-dimensional bump

The first test problem is chosen to verify that the present model indeed preserves the stationary steady flow with wet/dry fronts over uneven bottom. A bump is located at the centre of a frictionless closed square container, with the bed elevation given by [14,13]

$$b(x, y) = \max[0, 0.25 - 5 * ((x - 0.5)^2 + (y - 0.5)^2)]m, \quad 0 \leq x, y \leq 1m. \quad (57)$$

The similar example but in one-dimensional was used by other researchers (see e.g. [30,47,26]). Initial conditions are such that the water inside the container is at rest, and the water surface elevation is 0.1 m. So the bump is partially submerged. The steady state should be exactly preserved by numerical scheme. The initial water depth in each cell is computed by the other VFRs formulation proposed by Begnudelli and Sanders [8] since the water surface elevation is given. If the computed water depth is zero, the water level of the cell is set to be the lowest bed elevation of cell's three nodes. A simulation is carried out until $t = 500s$, using a mesh of 2500 triangular cells ($\xi = 0.04$ m). Fig. 2 shows the computed 3D water surface. Fig. 3(a) presents the water level and the bottom in cells versus the x -coordinate of the cell centroid along the line $y = 0.5$ m. Fig. 3(b) presents the unit discharge. Errors in terms of [8]

$$L_1(\eta) = \frac{1}{N_c} \sum_{i=1}^{N_c} |\eta_i - \tilde{\eta}_i| \quad L_1(Q) = \frac{1}{N_c} \sum_{i=1}^{N_c} |Q_i - \tilde{Q}_i|, \quad (58)$$

where $Q = h\sqrt{u^2 + v^2}$, $\tilde{\eta}$ and \tilde{Q} denote the exact solutions, N_c is the number of cells with positive water depth, are 8.48×10^{-14} m and 7.90×10^{-13} m²/s, respectively. In addition, the maximum relative mass error defined in (56) is 4×10^{-14} , which is sufficiently small to the level of round-off error of a double accuracy calculation. The results show that the stationary solutions are well maintained, and the differences between the numerical predictions and exact solutions are clearly due only to round-off errors of a double precision computation, verifying the well-balanced property.

4.2. Steady flow over a bump under different conditions

The goal of this test case is to investigate the ability of the present model to converge to a non-stationary steady state. The computational domain in the problem is a 25 m \times 1 m rectangular frictionless channel, and the bed elevation is specified as follows [29,8,23,42,51]

$$b(x, y) = \max[0, 0.2 - 0.05(x - 10)^2]. \quad (59)$$

Depending on the initial and the boundary conditions (Table 1), the flow may be subcritical (Case 2a) or transcritical, with or without a steady hydraulic jump (Case 2b and 2c, respectively). The three cases were simulated using a mesh of 2500 triangular cells ($\xi = 0.2$ m) to steady states. Solid slip conditions are imposed at the lateral walls of the channel. Fig. 4 shows the water surface

Table 2

Steady flow over a bump: L_1 error norms for free surface elevation and unit discharge.

Cases	$L_1(\eta)$ (m)	$L_1(hQ)$ (m ² /s)
2a	1.03×10^{-4}	5.88×10^{-4}
2b	7.39×10^{-4}	8.79×10^{-4}
2c	4.65×10^{-4}	8.25×10^{-4}

elevation and the unit discharge ($q = h\sqrt{u^2 + v^2}$) in cells versus the x -coordinate of the cell centroid along the centerline of the channel. The analytical solutions of water level are derived by using

Bernoulli's theorem (together with the momentum principle if a shock is present). Table 2 presents the errors of $L_1(\eta)$ and $L_1(hQ)$ evaluated according to (58). In Fig. 4, the computed water levels

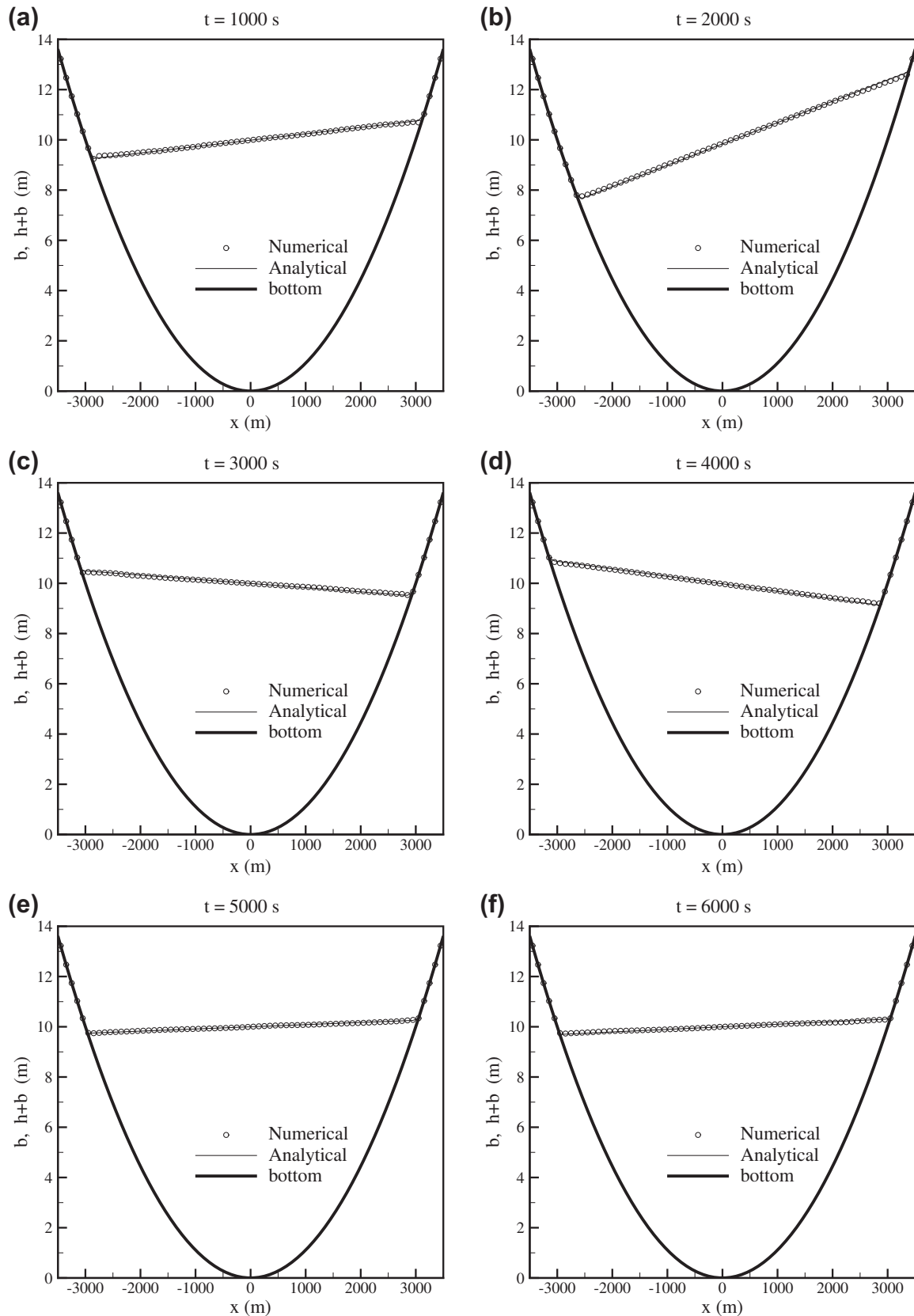


Fig. 5. Sloshing flow over a parabolic bottom with friction: water surface elevation along the line $y = 0$ at different output times: (a) $t = 1000$ s; (b) $t = 2000$ s; (c) $t = 3000$ s; (d) $t = 4000$ s; (e) $t = 5000$ s; (f) $t = 6000$ s.

match the exact solutions well, and the computed unit discharges generally agree with the exact solutions. The deviation between computed and exact values of the unit discharge bigger than that of the water level can be observed from Table 2: a very similar behavior can be found in Begnudelli and Sanders [8] and Aureli et al. [3]. Furthermore, the maximum relative mass errors defined in (56) are 3×10^{-14} , 4×10^{-14} and 4×10^{-14} for Case2a, 2b and 2c, respectively, which are accurate up to round-off error.

4.3. Moving shorelines in a parabolic bowl with friction

Analytical solutions of the one-dimensional nonlinear SWEs with a parabolic bottom were derived by Sampson et al. [35]. This provides a good benchmark test case for the present model in dealing with wet/dry fronts and source terms. This test case was investigated by other researchers (see e.g. [29,30,47,26]). Consider a rectangular computational domain $[-5000 \text{ m}, 5000 \text{ m}] \times [-5000 \text{ m}, 5000 \text{ m}]$, and the bed elevation is defined by

$$b(x, y) = h_0(x/a)^2, \quad (60)$$

where h_0 and a are constants to be specified later. The analytical water level, for the case with $\tau < p$, is given by

$$\begin{aligned} \eta(x, y, t) &= h_0 - \frac{e^{-\tau t/2}}{g} \left(Bs \cos st + \frac{\tau B}{2} \sin st \right) x \\ &\quad + \frac{a^2 B^2 e^{-\tau t}}{8g^2 h_0} \left[-s\tau \sin 2st + \left(\frac{\tau^2}{4} - s^2 \right) \cos 2st \right] - \frac{B^2 e^{-\tau t}}{4g}, \\ \eta(x, y, t) &= \max[\eta(x, y, t), b(x, y)], \end{aligned} \quad (61)$$

where $p = \sqrt{8gh_0}/a$ is the hump amplitude parameter; τ is the bed friction parameter; B is a given constant; and $s = \sqrt{p^2 - \tau^2}/2$. If $\tau = 0$, the flow is periodically oscillating. Otherwise, the sloshing flow is damped by bed friction as $t \rightarrow \infty$, and the location of the shorelines is $x = \pm a$.

The computational domain was triangulated with 40000 elements ($\xi = 100 \text{ m}$). Because the flow can not reach the boundaries, the boundary conditions have no effect on the numerical results and the solid slip conditions are employed in this case. The parameters are $a = 3000 \text{ m}$, $h_0 = 10 \text{ m}$, $\tau = 0.001 \text{ s}^{-1}$, and $B = 5 \text{ m/s}$. The initial condition is then defined by (61), together with $t = 0$, $u = v = 0$. In this problem, the $\tilde{\tau}^n$ in (41) is assumed to be a constant as τ . We run the simulation until $t = 6000 \text{ s}$. Fig. 5 shows the computed

water level along the line $y = 0$ at different times, compared with the analytical solutions: how it can be seen, a very good agreement is observed. The sloshing amplitude of water level is damping with increasing simulation time, due to the friction effect. The results validate the wetting and drying method of the present model, as well as the source terms treatments. Fig. 6 shows the comparison between numerical and analytical solutions for water depth at points $(-2750; 0)$, $(-50; 0)$, and $(2750; 0)$. Fig. 7 shows the computed results of unit discharge in the x -direction at these points. An averaged relative error is calculated for the water surface elevation, to give overall quantitative information about the accuracy of the numerical predictions. The averaged relative error is estimated as

$$L_1(\eta) = \frac{1}{N_c} \sum_{i=1}^{N_c} \left| \frac{\eta_i - \tilde{\eta}_i}{\tilde{\eta}_i} \right|, \quad (62)$$

where η_i and $\tilde{\eta}_i$ are the numerical and analytical water surface elevation in cell i , respectively. Fig. 8 presents the time evolution of the averaged relative error for water surface elevation. In addition, the maximum relative mass error defined in (56) is 3×10^{-14} , which is accurate up to the level of round-off error.

4.4. Drain on a non-flat bottom

Due to the simultaneously involving moving shock, transcritical flow and wet/dry fronts over a non-flat bottom, this transient flow problem is extremely severe for numerical schemes. The problem domain, bed elevation and computational meshes are the same as those in Section 4.2. The initial conditions are $\eta(x, y) = 0.5$, $u(x, y) = v(x, y) = 0$. The western boundary and the lateral walls of the channel are solid slip conditions while the eastern boundary is an outlet condition on a flat dry bed (refer to [15] for details). The flow reaches a stationary state with $\eta = 0.2 \text{ m}$ to the left of the bump and $h = 0$ to its right. This problem may be also found in [47,26,20].

We run the simulation until $t = 1000 \text{ s}$. The initial water surface profile and numerical results obtained at times $t = 10, 20, 50, 100$, and 1000 s along the line $y = 0.5 \text{ m}$ are shown in Fig. 9, and can be directly compared with those presented in [47,26,20]. The numerical solutions reflect the anticipant flow pattern well and converge to the expected steady state. Moreover, the maximum relative

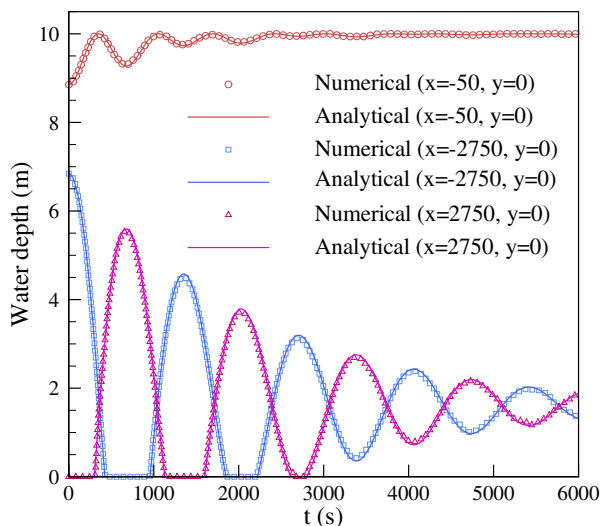


Fig. 6. Sloshing flow over a parabolic bottom with friction: comparison between numerical and analytical results for water depth at points $(-2750; 0)$, $(-50; 0)$, and $(2750; 0)$.

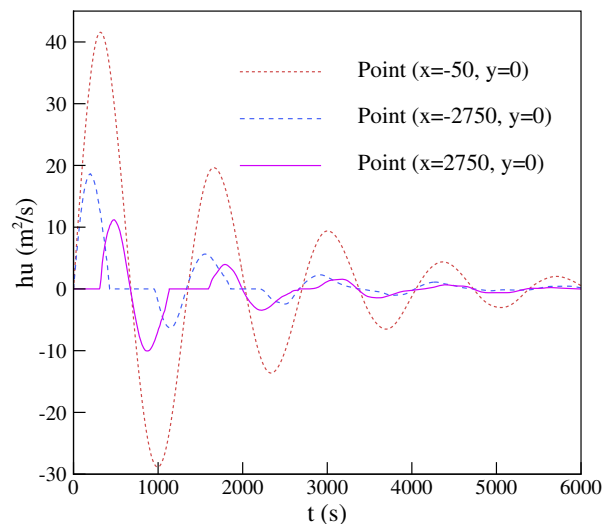


Fig. 7. Sloshing flow over a parabolic bottom with friction: numerical results for unit discharge in the x -direction at points $(-2750; 0)$, $(-50; 0)$, and $(2750; 0)$.

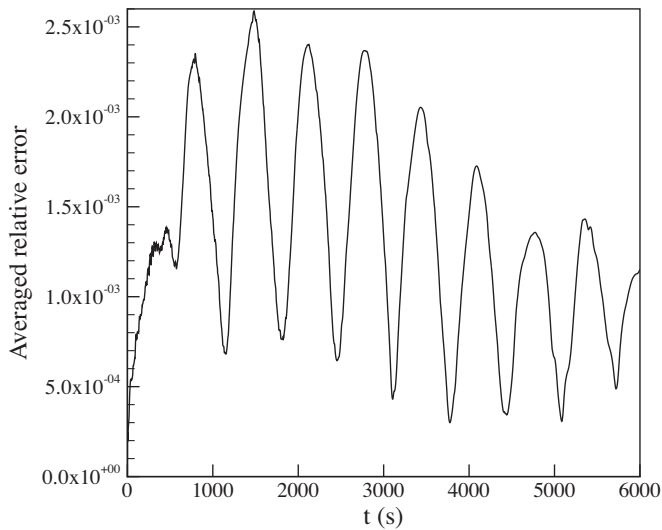


Fig. 8. Sloshing flow over a parabolic bottom with friction: time evolution of the averaged relative error for water surface elevation.

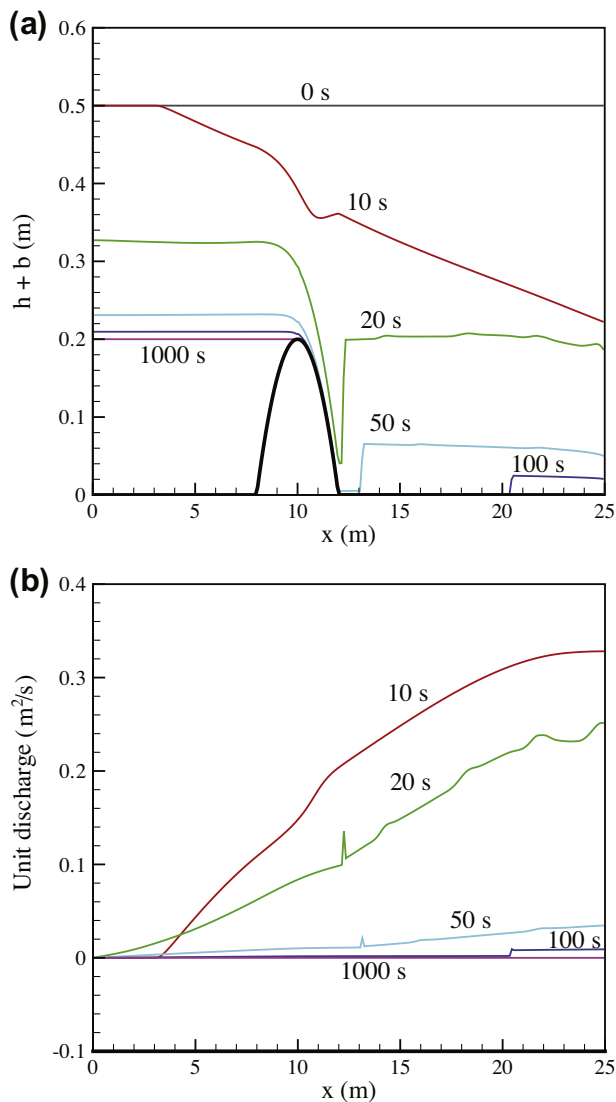


Fig. 9. Drain on a non-flat bottom: (a) water level and (b) unit discharge profiles along the line $y = 0.5$ m at different output times.

mass error defined in (56) is 4×10^{-14} , which is accurate up to round-off error.

4.5. Dam-break flood through a trapezoidal breach with friction

To validate the present model in an application involving friction, a flood wave produced by a partial dam-break through a trapezoidal breach is studied. The results obtained by Betcheler et al. [10] in a dam-break experiment that represents the propagation of a flood wave are previously simulated by Brufau and Garcia-Navarro [13] and Begnudelli and Sanders [8]. The experimental configuration consists of a reservoir 7 m wide and 2 m long separated by a dam 7 m wide and 0.4 m long from a platform 7 m wide and 5 m long (see Figs. 7 and 8 of Brufau and Garcia-Navarro's [13] paper). The dam is numerically represented as an elevation of the bottom of the platform, and includes a trapezoidal breach that is

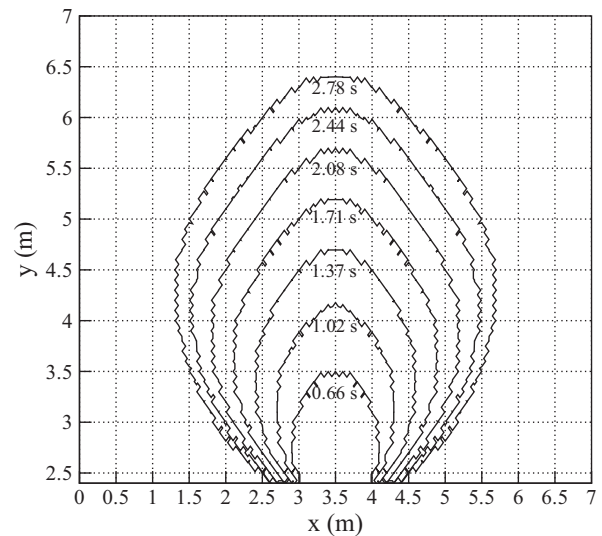


Fig. 10. Trapezoidal dam-break problem: time advancing curves of the flood wave front.

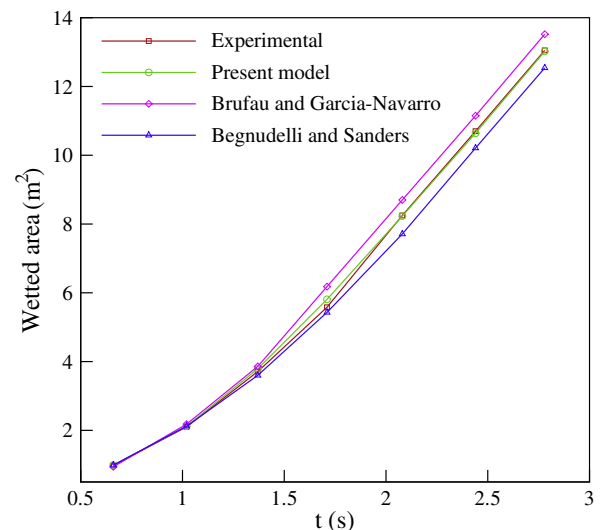


Fig. 11. Trapezoidal dam-break problem: time evolution of the wetted area downstream of the dam.

Table 3

Dam-break flood through a trapezoidal breach: Experimental and numerical results comparison on wetted area of the advancing flood wave fronts downstream of the dam.

Times (s)	Wetted area (m ²)				Relative error (%)		
	Experimental data	Present model	Brufau and Garcia-Navarro	Begnudelli and Sanders	Present model	Brufau and Garcia-Navarro	Begnudelli and Sanders
0.66	0.98	0.99	0.94	0.99	1.0	4.1	1.0
1.02	2.10	2.12	2.18	2.12	1.0	3.8	1.0
1.37	3.71	3.79	3.86	3.60	2.2	4.0	3.0
1.71	5.58	5.81	6.18	5.43	4.1	10.8	2.7
2.08	8.25	8.23	8.70	7.71	0.2	5.5	6.5
2.44	10.70	10.64	11.15	10.21	0.6	4.2	4.6
2.78	13.05	13.02	13.52	12.54	0.2	3.6	3.9

suddenly opened at time $t = 0$ s, producing a partial dam-break, and propagating a flood wave across the platform. The three boundaries of the platform are free outlet, and the three boundaries of the reservoir are solid walls.

Initial conditions are 0.2 m water depth inside the reservoir at rest and dry bed in the rest. Manning's roughness coefficient is $n = 0.01 \text{ s m}^{-1/3}$. Using an unstructured grid of 20720 cells ($\xi = 0.1 \text{ m}$), flow is simulated and the time advancing curves of the flood wave fronts at times $t = 0.66, 1.02, 1.37, 1.71, 2.08, 2.44$ and 2.78 s are shown in Fig. 10. It can be observed that after the dam break, water is symmetrically expanded around the main axis. These results are similar to the experimental records of Betcheler et al. [10] and the simulated results of Brufau and Garcia-Navarro [13]. The wetted area downstream of the dam during the advancing of the flood fronts is measured for comparison with the experimental records of Betcheler et al. [10] and the simulated results of Brufau and Garcia-Navarro [13] and Begnudelli and Sanders [8]. The results are presented in Table 3 and Fig. 11, and illustrate that model predictions compare well with experimental data. The relative error values of the present model remain below 5%. It should be noted that, as demonstrated by Begnudelli and Sanders [8], these errors are undoubtedly influenced by the structure and resolution of grids used by these models, not only the schemes. Furthermore, the maximum relative mass error defined in (56) is 5×10^{-14} , which is accurate up to the level of round-off error.

4.6. Shallow water sloshing in a two-dimensional parabolic basin without friction

To verify the capability of the proposed method of accurately modeling flows in the presence of 2D wet/dry fronts on non-flat topographies, Thacker's periodic flow with a planar free surface [40] is investigated. This test case is extremely difficult for numerical models. The bed elevation is described by

$$b(x, y) = \frac{h_0}{a^2}(x^2 + y^2), \quad (63)$$

where h_0 and a are positive constants. The equations of this periodic motion are given by [40]:

$$\begin{aligned} h(x, y, t) &= \max \left[0, \frac{\sigma h_0}{a^2} (2x \cos(wt) + 2y \sin(wt) - \sigma) + h_0 - b(x, y) \right] \\ u &= -\sigma w \sin(wt) \quad v = -\sigma w \cos(wt), \end{aligned} \quad (64)$$

where σ is a constant that determines the amplitude of the motion; $w = \sqrt{2gh_0}/a$ is the frequency of the rotation around the center of the basin. The movement of the water is restricted within a circular area of radius $a + \sigma$. The solutions are only valid when $\sigma < a^2/2h_0$ since the SWEs are based on the assumption of a hydrostatic pressure distribution.

The test is performed in a square domain $[-10000 \text{ m}, 10000 \text{ m}] \times [-10000 \text{ m}, 10000 \text{ m}]$ with $h_0 = 10 \text{ m}$, $a = 8025.5 \text{ m}$,

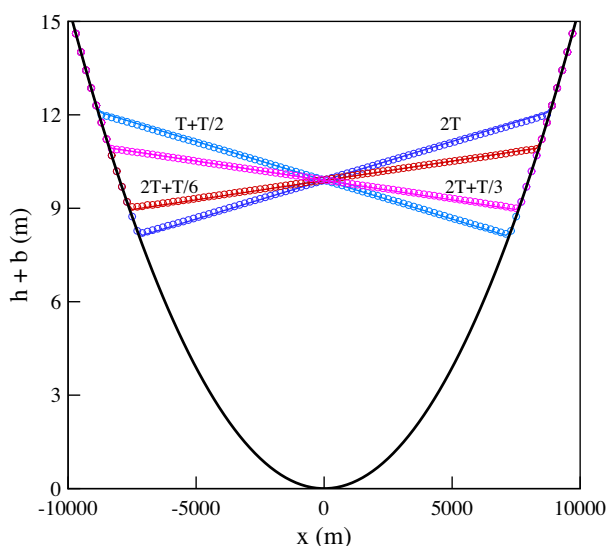


Fig. 12. Thacker's test with planar surface: water surface elevation at different output times. Analytical solution and bottom elevation are given by solid lines; numerical results are given by circle.

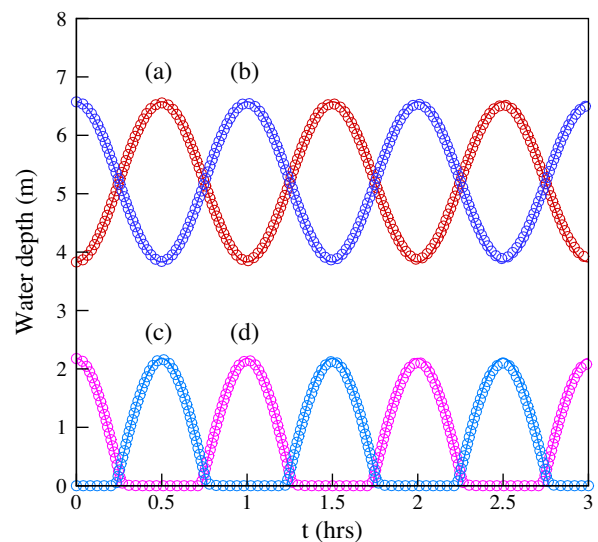


Fig. 13. Thacker's test with planar surface: comparison between numerical and analytical results for water depth at points (a): $(-5500, 0)$; (b): $(5500, 0)$; (c): $(-7900, 0)$ and (d): $(7900, 0)$. Analytical solutions are given by solid lines; numerical results are given by circle.

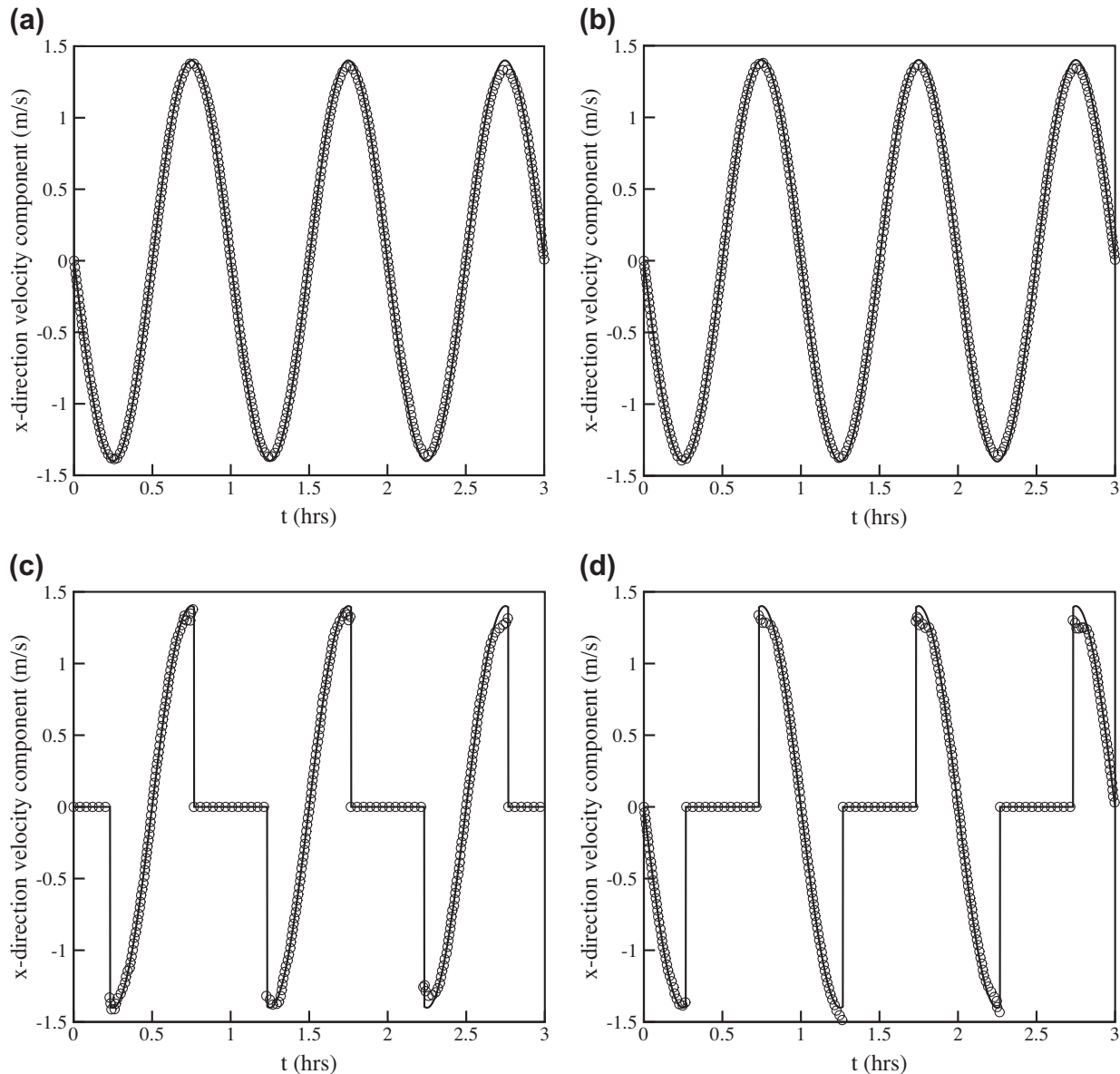


Fig. 14. Thacker's test with planar surface: comparison between numerical and analytical results for velocity component in the x-direction at points (a): $(-5500;0)$; (b): $(5500;0)$; (c): $(-7900;0)$ and (d) $(7900;0)$. Analytical solutions are given by solid lines; numerical results are given by circle.

and $\sigma = a/10$. The oscillation period is $T = 2\pi/\omega = 3600$ s. These settings were proposed by Liang [31] and are used here. The computational domain was triangulated with 40000 elements ($\xi = 200$ m). The basin dimensions are such that the water never reaches the boundaries, therefore we can pick open boundary conditions and they have no impact on the numerical results. The solutions according to (64) evaluated at $t = 0$ are used as the initial conditions. We run the simulation until time $3T$. Fig. 12 shows a very good agreement between numerical and analytical solutions for free surface along the line $y = 0$ at several sample output times. The moving shoreline is accurately simulated with no signs of amplified spurious oscillations. Fig. 13 shows the comparison between numerical and analytical solutions of time history of water depth in three periods at points $(-5500;0)$, $(5500;0)$, $(-7900;0)$ and $(7900;0)$, and the comparisons of corresponding velocity component in the x-direction are shown in Fig. 14. The first two points remain wet all the time, whereas the last two points get wet and dry during the periodic motion. In Fig. 13, numerical predictions

match perfectly with the analytical solutions. Slight numerical dissipation can be observed in Fig. 13, and it increases with time throughout the simulation. In Fig. 14, the computed results of velocity component in the x-direction again agree well with the analytical solutions. However, little deviations can be found in Figs. 14(c) and (d), at where the wetting or drying occurs. In addition, the maximum relative mass error defined in (56) is 2×10^{-14} , which is accurate up to round-off error.

4.7. Case study: collapse of the dam on Paute River

In order to test the applicability of the present model to real case studies characterized by an irregular topography, the flooding after the instantaneous and complete collapse of the dam, which was created by the failure of a mountainside, on Paute River in southern highland Ecuador is presented. Topography and mesh data about the computation domain are available from BreZo [36]. Fig. 15 illustrates the plan view of the bed elevation together

with the locations of the surveyed points. The computational domain was triangulated with 74224 elements, and triangles were more densely organized along the river. Free outgoing conditions are imposed along all boundaries. At the initial time, the static condition corresponding to the constant water level of 2362 m is imposed in the upstream of the dam, whereas the bed is set to be dry in the downstream. The uniformly distributed Manning roughness coefficient is set at $0.033 \text{ m}^{-1/3} \text{ s}$.

We run the simulation until 6000 s after the breaking. As it can be seen from Fig. 16 of the flow field at minute 3 after the breaking, the present model is able to preserve the static condition in the region not yet reached by the wave propagating along upstream. Fig. 17 shows the simulated hydrographs given by the present scheme. The BreZo model is also run for comparison, and results are plotted in Fig. 17. A fixed time step of 0.2 s and LTS level of 1 are selected for the BreZo. It can be seen from Fig. 17, upstream water release simulated by the present model is faster than that of the BreZo. Besides, the flood predicted by the proposed model arrives slightly earlier at the downstream surveyed points. These differences may be partially due to that the BreZo is formally first-order accurate, whereas the proposed model is second-order accurate for fully wetted areas, and therefore should be less dissipative. Furthermore, Figs. 17(c) and (d) show that the current model presents more oscillating predictions than those produced by BreZo. In order to assess these oscillations, simulations are carried out with two smaller Courant number of $C_r = 0.4$ and $C_r = 0.1$ (and thus smaller time steps). The corresponding water level processes at the surveyed points are also plotted in Fig. 17, which shows the generally identical results when $C_r = 0.8, 0.4$, and 0.1 . So it can be concluded that the Courant number hardly affects the final accuracy of the obtainable results, and the proposed model is not sensitive to the time steps. Thus the results computed by the presented model are stable. We think that these oscillations do not affect the applicability of the results, since the arriving time and the maximum water level are two more important factors in dam-break simulation. Moreover, results of [39] are plotted in Fig. 17 for comparison. It can be seen from Fig. 17 that water level processes of [39] are much smoother than those of the present model. Besides, upstream water release of [39] is the fastest, whereas the corresponding flood arrives later than others at both downstream surveyed points (e) and (f), deviating from our expectation that it would arrive earliest. A possible reason for this deviation is that the flux corrections used in [39] lead to the momentum nonconservation problem, as discussed in the

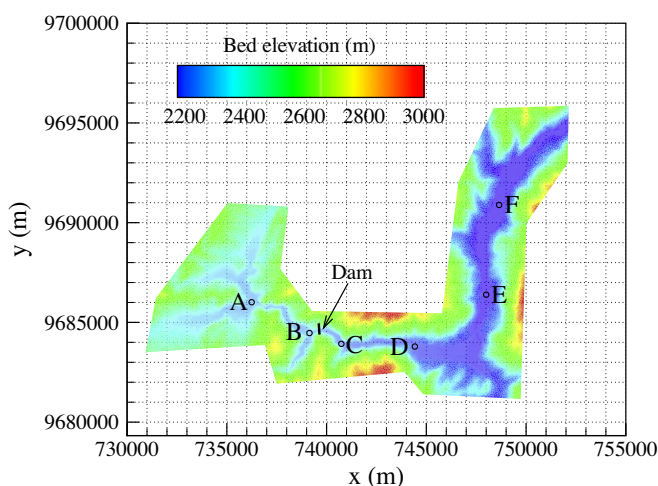


Fig. 15. Real field case study: plan view of the bed elevation plot and the locations of surveyed points.

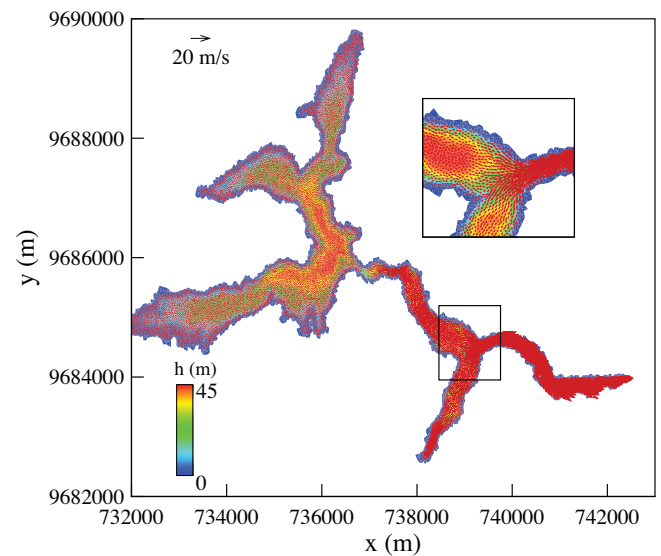


Fig. 16. Real field case study: water stage with velocity vector at minute 3 after the breaking.

Introduction. On the other hand, quantitative discrepancies in results between different numerical models are also reasonable. Since no true data is available for results validation, it may be concluded that models under an integral and rational theory framework should lead to reliable results [33,18]. Overall, the water level processes predicted by those models are qualitatively consistent with each other, but the results predicted by the present model are most reliable, as the present model uses the new formulation of SWEs and thus preserves the C-property without the need for flux corrections, i.e. the present model is under an integral and rational theory framework and thus predicts reliable results. The proposed model and the BreZo model are both run on a PC with a Core 2 2.4 GHz processor, and the run time was about 389 min ($C_r = 0.8$) and 36 min, respectively. The run time of the proposed model is longer than that of the BreZo, because not only the Java code used by the proposed model is not so efficient as the Fortran code used by the BreZo, but also the two-stage Runge–Kutta scheme adopted by the proposed model needs more computation consumption than the first-order method [37] used by the BreZo model. Moreover, very small negative water depth has been predicted during the simulation, and the maximum relative mass error defined in (56) is 2×10^{-10} , which is very low and thus acceptable for practical applications.

To test the influence of mass nonconservation on the simulated results, we also implemented another empirical technique to deal with the predicted negative depths, i.e. not only the computed water depths lower than zero are set at zero, but also the corresponding amount of mass gain is subtracted from the neighboring cells with enough water to guarantee mass conservation. We again run the simulation until 6000 s with $C_r = 0.8$. The resulting maximum relative mass error defined in (56) is 4×10^{-14} , indicating that the mass conservation is well preserved. The corresponding water level processes at the surveyed points, labeled by “Mass Conservation”, are also plotted in Fig. 17, which shows the mostly consistent results.

5. Conclusions

A new formulation of the SWEs, which is different from the classical form in the formulation of hydrostatic pressure and bottom slope effects and their division between fluxes and source terms, is presented as the basis of a well-balanced Godunov-type finite

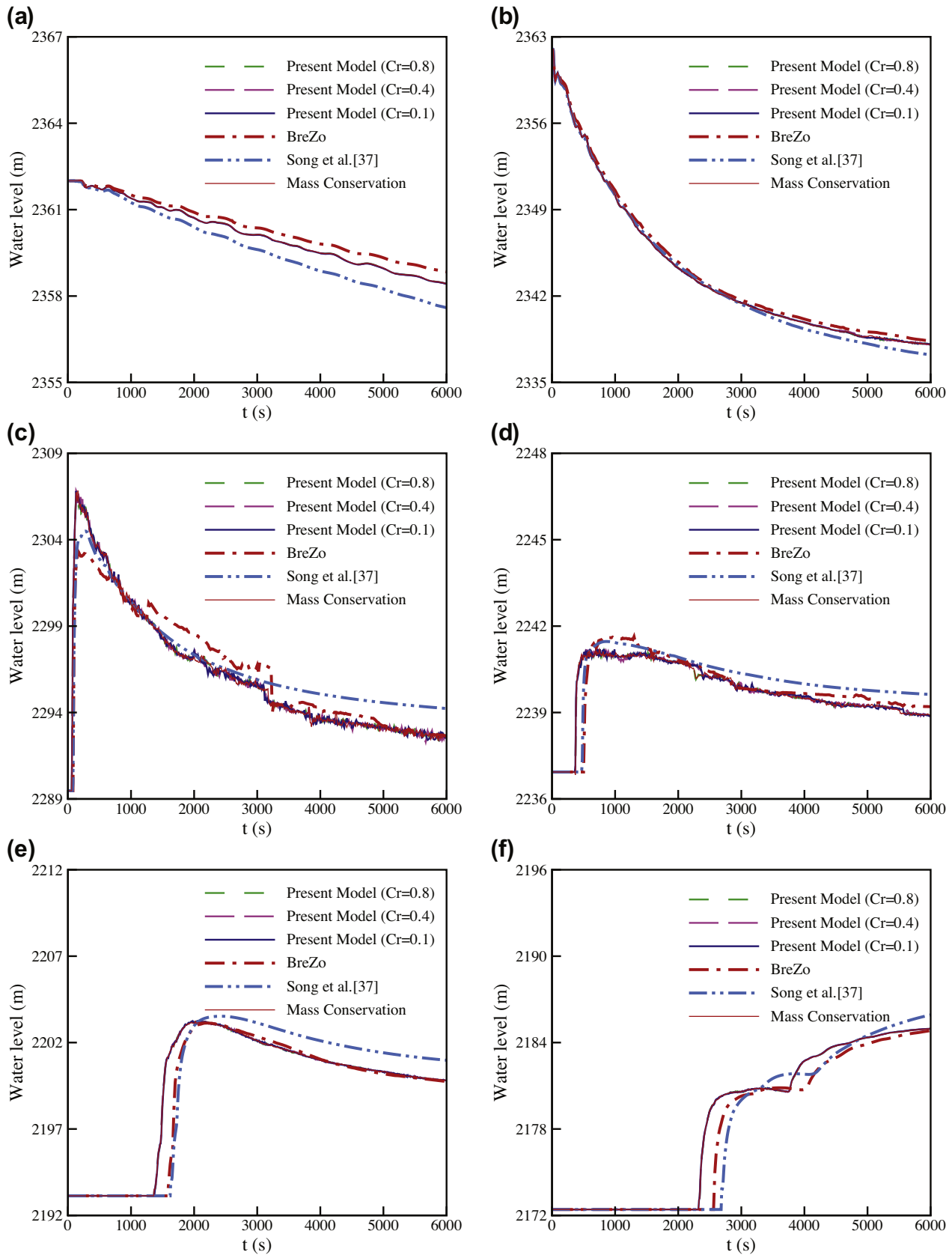


Fig. 17. The computed hydrographs comparison at different surveyed points: (a) at surveyed point A; (b) at surveyed point B; (c) at surveyed point C; (d) at surveyed point D; (e) at surveyed point E; (f) at surveyed point F.

volume scheme. The new formulation can essentially eliminate the need for momentum flux corrections, providing a robust alterna-

tive to the classical form. In other words, using HLLC solver to calculate numerical fluxes of the new formulation of SWEs together

with the centered discretization of the bed slope source terms enables the scheme to exactly preserve the stationary solutions on irregular topographies (C-property) without any additional correction terms.

Besides, the new formulation presented in this paper also slightly differs from the pre-balanced form proposed by Liang and Marche [30], i.e. the former uses water depth as a flow variable to update solutions and the latter uses water level correspondingly. It should be noted that, when the bed elevation is defined at the centroid of each cell and the terrain within each cell is assumed to be flat, the use of either water level or water depth as a flow variable to update solutions does not impact the mass conservation of the formulation. However, the sloping bottom model, in which the water depth of each cell is defined to be the ratio of the water volume to the cell area, whereas the water level is defined to be the free surface elevation in the wetted portion of the cell [8], is incorporated into the present scheme to provide a robust approach for wetting and drying applications. In the framework of sloping bottom model, when the topography of problem domain is highly irregular and relatively coarse grids are used for computation, water depth rather than water level should be used as a flow variable for solution updating to preserve the mass conservation in both fully and partially submerged cells. This is the main motivation of deriving the new formulation in this work.

Negative water depths could be predicted in the proposed model. After the implement of the wet/dry fronts sharpening method, the computed water depths lower than zero are set at zero, and the corresponding velocities are also set at zero. This procedure leads to a gain of mass, which is a function that increases with time. The prediction of negative depths is a problem of model only when the mass error from negative depths becomes too large to be accepted, and if so, an error correction step should be implemented to preserve mass conservation. Results of all simulations presented in this paper show that the magnitude of negative water depths is very small even when the topography is highly irregular. As a result, as well as due to the relatively short simulation time, the mass errors in all simulations are very low. It should be noted that long enough run time would lead to an unacceptable mass gain, and if so, the error correction step should be used.

The model presented in this paper is robust for several reasons including: (1) it represents numerically irregular terrain with second-order accuracy; (2) it preserves the C-property without the need for momentum flux corrections; (3) all flow regimes (subcritical, supercritical, transcritical, discontinuities, etc.) are accurately predicted; (4) the wetting and drying processes over irregular terrain are reproduced effectively; (5) the friction terms are solved by a semi-implicit scheme that does not invert the direction of velocity components; (6) highly-unsteady, rapidly-varying dam-break flows over real topography are successfully simulated.

The effectiveness and robustness of the proposed model are validated through its application to extensive numerical examples involving steady and unsteady flow, non-flat bed, 2D wet/dry fronts, and friction effect. The comparison between numerical and reference results demonstrates the well-balanced property, accuracy, and robust tracking of wet/dry fronts of the proposed model. Moreover, the case study concerning the flooding over real topography after the collapse of the dam on Paute River confirms the applicability of the present model for field-scale applications. In the near future, we plan to use the proposed model to reproduce the historical dam-break flood for comparison to the true data.

Acknowledgements

The authors are grateful to the anonymous reviewers for providing many constructive suggestions. This work was supported by a grant from the National Basic Research Program of China

(Project No. 2007CB714107), a grant from the Key Projects in the National Science & Technology Pillar Program (Project No.2008-BAB29B08), and a grant from the Special Research Foundation for the Public Welfare Industry of the Ministry of Science and Technology and the Ministry of Water Resources (Project No.200701008).

Appendix A

In this appendix we provide a brief proof of the need of extra momentum flux corrections to maintain well-balanced solution when the traditional shallow water equations combined with surface gradient methods is used. We provide this for completeness to the reader. It should be noted that the following analysis is based on the sloping triangular cell.

In the case of a fully wetted cell C_i , the following relations is true in the stationary flow field situation with constant water level η for the k th edge ($k = 1, 2, 3$):

$$\eta_{i,k} = h_{i,k} + b_{i,k} = \eta \quad u_{i,k} = v_{i,k} = 0, \quad (\text{A.1})$$

where $\eta_{i,k}$, $h_{i,k}$, $u_{i,k}$, and $v_{i,k}$ are the reconstructed values at the middle point of the edge; $b_{i,k}$ is the bed elevation at the middle point of the edge.

Then for traditional shallow water equations given by (1) and (2), the numerical flux is:

$$\sum_{k=1}^3 \mathbf{F}_{i,k} \cdot \mathbf{n}_{i,k} L_{i,k} = \begin{bmatrix} 0 \\ \sum_{k=1}^3 \frac{1}{2} g h_{i,k}^2 L_{i,k} n_{i,k}^x \\ \sum_{k=1}^3 \frac{1}{2} g h_{i,k}^2 L_{i,k} n_{i,k}^y \end{bmatrix}. \quad (\text{A.2})$$

Note that (A.2) reflects the hydrostatic pressure difference, and is independent of the Riemann solver being used. Under the stationary flow condition, and using surface gradient method gives

$$h_{i,k} = \eta - b_{i,k} \quad (h_1)_{i,k} = \eta - (b_1)_{i,k} \quad (h_2)_{i,k} = \eta - (b_2)_{i,k} \\ b_{i,k} = [(b_1)_{i,k} + (b_2)_{i,k}]/2.$$

So

$$h_{i,k} = [(h_1)_{i,k} + (h_2)_{i,k}]/2. \quad (\text{A.4})$$

Substituting of (A.4) into (A.2) and regarding the second component (i.e. the x -direction momentum flux) gives

$$\left(\sum_{k=1}^3 \mathbf{F}_{i,k} \cdot \mathbf{n}_{i,k} L_{i,k} \right)^2 = \sum_{k=1}^3 \frac{1}{2} g h_{i,k}^2 L_{i,k} n_{i,k}^x \\ = \frac{1}{2} g \sum_{k=1}^3 \frac{[(h_1)_{i,k} + (h_2)_{i,k}]^2}{4} L_{i,k} n_{i,k}^x. \quad (\text{A.5})$$

On the other hand, for traditional shallow water equations, the bed slope term approximation in the x -direction is:

$$S_{i,0x} = - \int_{C_i} g h \frac{\partial b}{\partial x} d\Omega = \int_{C_i} \frac{\partial}{\partial x} \left(\frac{1}{2} g h^2 \right) d\Omega = \oint_{\partial C_i} \frac{1}{2} g h^2 n_x dl \\ = \sum_{k=1}^3 \frac{1}{2} g \left(\int_{\varepsilon=0}^{L_{i,k}} h_{i,k}^2 d\varepsilon \right) n_{i,k}^x \\ = \frac{1}{2} g \sum_{k=1}^3 \frac{(h_1)_{i,k}^2 + (h_1)_{i,k} (h_2)_{i,k} + (h_2)_{i,k}^2}{3} L_{i,k} n_{i,k}^x, \quad (\text{A.6})$$

where $(h_1)_{i,k}$ and $(h_2)_{i,k}$ are the water depths at the two endpoints of the edge k of C_i . Note that a more directly approximation of bed slope term $S_{i,0x} = -g h_i (\partial b / \partial x)_i \Omega_i$ is the same as (A.6) after some algebraic transformation. Subtracting (A.5) from (A.6) gives

$$-\left(\sum_{k=1}^3 \mathbf{F}_{i,k} \cdot \mathbf{n}_{i,k} L_{i,k}\right)^2 + S_{i,0x} = \frac{1}{2} g \sum_{k=1}^3 \frac{[(h_1)_{i,k} - (h_2)_{i,k}]^2}{12} L_{i,k} \mathbf{n}_{i,k}^x. \quad (\text{A.7})$$

(A.7) reveals the unbalancing between the flux-gradient and bed slope source term, and further indicates the need of extra momentum flux correction, which is given by the right side of (A.7), to maintain well-balanced solution in the x -direction. A similar analysis can be applied in the y -direction momentum equation.

References

- [1] Arega F, Sanders BF. Dispersion model for tidal wetlands. *ASCE J Hydr Eng* 2004;130(8):739–54.
- [2] Ancey C, Iverson RM, Rentschler M, Denlinger RP. An exact solution for ideal dam-break floods on steep slopes. *Water Resour Res* 2008;44(1):W01430.
- [3] Aureli F, Maranzoni A, Mignosa P, Ziveri C. A weighted surface-depth gradient method for the numerical integration of the 2D shallow water equations with topography. *Adv Water Res* 2008;31(7):962–74.
- [4] Balzano A. Evaluation of methods for numerical simulation of wetting and drying in shallow water flow models. *Coastal Eng* 1998;34(1–2):83–107.
- [5] Begnudelli L, Sanders BF, Bradford SF. Adaptive Godunov-based model for flood simulation. *ASCE J Hydr Eng* 2008;134(6):714–25.
- [6] Begnudelli L, Sanders BF. Conservative wetting and drying methodology for quadrilateral grid finite-volume models. *ASCE J Hydr Eng* 2007;133(3):312–22.
- [7] Begnudelli L, Sanders BF. Simulation of the St. Francis dam-break flood. *ASCE J Eng Mech* 2007;133(11):1200–12.
- [8] Begnudelli L, Sanders BF. Unstructured grid finite-volume algorithm for shallow-water flow and scalar transport with wetting and drying. *ASCE J Hydr Eng* 2006;132(4):371–84.
- [9] Bermudez A, Vazquez ME. Upwind methods for hyperbolic conservation laws with source terms. *Comput Fluids* 1994;23(8):1049–71.
- [10] Betcheler W, Kulisch H, Nujic M. 2-D dam-break flooding waves comparison between experimental and calculated results. *Int Rep Inst of Hydromech and Hydr, Univ of the Federal Armed Forces, Munich*, 1999.
- [11] Bradford SF, Sanders BF. Finite-volume model for shallow-water flooding of arbitrary topography. *ASCE J Hydr Eng* 2002;128(3):289–98.
- [12] Brown JD, Spencer T, Moeller I. Modeling storm surge flooding of an urban area with particular reference to modeling uncertainties: a case study of Canvey Island, United Kingdom. *Water Resour Res* 2007;43(6):W06402.
- [13] Brufau P, Garcia-Navarro P. Unsteady free surface flow simulation over complex topography with a multidimensional upwind technique. *J Comput Phys* 2003;186(2):503–26.
- [14] Brufau P, Vazquez-Cendon ME, Garcia-Navarro P. A numerical model for the flooding and drying of irregular domains. *Int J Numer Methods Fluids* 2002;39(3):247–75.
- [15] Buffard T, Gallouet T, Herard JM. A sequel to a rough Godunov scheme: application to real gases. *Comput Fluids* 2000;29(7):813–47.
- [16] Canestrelli A, Dumbser M, Siviglia A, Toro EF. Well-balanced high-order centered schemes on unstructured meshes for shallow water equations with fixed and mobile bed. *Adv Water Res* 2010;33(3):291–303.
- [17] Canestrelli A, Siviglia A, Dumbser M, Toro EF. Well-balanced high-order centred schemes for non-conservative hyperbolic systems. Applications to shallow water equations with fixed and mobile bed. *Adv Water Res* 2009;32(6):834–44.
- [18] Cao Z, Carling PA. Mathematical modelling of alluvial rivers: reality and myth. Part 2: Special issues. *Water Maritime Eng ICE* 2002;154(4):297–307.
- [19] Fraccarollo L, Toro EF. Experimental and numerical assessment of the shallow water model for two-dimensional dam-break type problems. *J Hydr Res* 1995;33(6):843–64.
- [20] Gallardo JM, Pares C, Castro M. On a well-balanced high-order finite volume scheme for shallow water equations with topography and dry areas. *J Comput Phys* 2007;227(1):574–601.
- [21] Gallegos HA, Schubert JE, Sanders BF. Two-dimensional, high-resolution modeling of urban dam-break flooding: a case study of Baldwin Hills, California. *Adv Water Res* 2009;32(8):1323–35.
- [22] George DL. Adaptive finite volume methods with well-balanced Riemann solvers for modeling floods in rugged terrain: Application to the Malpasset dam-break flood (France, 1959). *Int J Numer Methods Fluids* 2010 (doi:10.1002/fld.2298).
- [23] George DL. Augmented Riemann solvers for the shallow water equations over variable topography with steady states and inundation. *J Comput Phys* 2008;227(6):3089–113.
- [24] Harten A, Lax PD, Van Leer B. On upstream differencing and Godunov-type schemes for hyperbolic conservation-laws. *SIAM Rev* 1983;25(1):35–61.
- [25] Hubbard ME. Multidimensional slope limiters for MUSCL-type finite volume schemes on unstructured grids. *J Comput Phys* 1999;155(1):54–74.
- [26] Kesserwani G, Liang Q. Well-balanced RKDG2 solutions to the shallow water equations over irregular domains with wetting and drying. *Comput Fluids* 2010;39(10):2040–50.
- [27] Kramer T, Jozsa J. Solution-adaptivity in modelling complex shallow flows. *Comput Fluids* 2007;36(3):562–77.
- [28] LeVeque RJ. Finite volume methods for hyperbolic problems. Cambridge: Cambridge University Press; 2002.
- [29] Liang Q, Borthwick AGL. Adaptive quadtree simulation of shallow flows with wet-dry fronts over complex topography. *Comput Fluids* 2009;38(2):221–34.
- [30] Liang Q, Marche F. Numerical resolution of well-balanced shallow water equations with complex source terms. *Adv Water Res* 2009;32(6):873–84.
- [31] Liang Q. Flood simulation using a well-balanced shallow flow model. *ASCE J Hydr Eng* 2010;136(9):669–75.
- [32] Nikolos IK, Delis AI. An unstructured node-centered finite volume scheme for shallow water flows with wet/dry fronts over complex topography. *Comput Meth Appl Mech Eng* 2009;198(47–48):3723–50.
- [33] Oreskes N, Shrader-Frechette K, Belitz K. Verification, validation, and confirmation of numerical models in the earth sciences. *Science* 1994;263:641–6.
- [34] Pan C, Lin B, Mao X. Case study: numerical modeling of the tidal bore on the Qiantang River, China. *ASCE J Hydr Eng* 2007;133(2):130–8.
- [35] Sampson J, Easton A, Singh M. Moving boundary shallow water flow above parabolic bottom topography. *ANZIAM J* 2006;47(EMAC2005):C373–87.
- [36] Sanders BF, Begnudelli L. BreZo: a hydrodynamic flood simulation algorithm. Available from: <<http://sanders.eng.uci.edu/brezo.html>>.
- [37] Sanders BF. Integration of a shallow water model with a local time step. *J Hydr Res* 2008;46(4):466–75.
- [38] Shewchuk JR. Triangle: engineering a 2D quality mesh generator and Delaunay triangulator. *Lect Notes Comput Sci* 1996;1148:203–22. <<http://www.cs.cmu.edu/~quake/triangle.html>>.
- [39] Song L, Zhou J, Li Q, Yang X, Zhang Y. An unstructured finite volume model for dam-break floods with wet/dry fronts over complex topography. *Int J Numer Methods Fluids* 2010. doi:10.1002/fld.2397.
- [40] Thacker WC. Some exact solutions to the nonlinear shallow-water wave equations. *J Fluid Mech* 1981;107:499–508.
- [41] Toro EF. Shock-capturing methods for free-surface shallow flows. Chichester: John Wiley & Sons; 2001.
- [42] Valiani A, Begnudelli L. Divergence form for bed slope source term in shallow water equations. *ASCE J Hydr Eng* 2006;132(7):652–65.
- [43] Valiani A, Caleffi V, Zanni A. Case study: Malpasset dam-break simulation using a two-dimensional finite volume method. *ASCE J Hydr Eng* 2002;128(5):460–72.
- [44] Van Leer B. Towards the ultimate conservative difference scheme. V.A second-order sequel to Godunov's method. *J Comput Phys* 1979;32(1):101–36.
- [45] Wang X, Cao Z, Pender G, Neel S. Numerical modeling of flood flows over irregular topography. *Water Management, ICE* 2010;163(WM5):255–65.
- [46] Wu C, Huang G, Zheng Y. Theoretical solution of dam-break shock wave. *ASCE J Hydr Eng* 1999;125(11):1210–5.
- [47] Xing Y, Zhang X, Shu C-W. Positivity-preserving high-order well-balanced discontinuous Galerkin methods for the shallow water equations. *Adv Water Res* 2010. doi:10.1016/j.advwatres.2010.08.005.
- [48] Yoon TH, Kang SK. Finite volume model for two-dimensional shallow water flows on unstructured grids. *ASCE J Hydr Eng* 2004;130(7):678–88.
- [49] Yue Z, Cao Z, Li X, Che T. Two-dimensional coupled mathematical modeling of fluvial processes with intense sediment transport and rapid bed evolution. *Sci Chin (Ser G)* 2008;51(9):1427–38.
- [50] Zhao DH, Shen HW, Tabios III GQ, Lai JS, Tan WY. Finite-volume two-dimensional unsteady-flow model for river basins. *ASCE J Hydr Eng* 1994;120(7):863–83.
- [51] Zhou JG, Causon DM, Mingham CG, Ingram DM. The surface gradient method for the treatment of source terms in the shallow-water equations. *J Comput Phys* 2001;168(1):1–25.
- [52] Zia A, Banihashemi MA. Simple efficient algorithm (SEA) for shallow flows with shock wave on dry and irregular beds. *Int J Numer Methods Fluids* 2008;56(11):2021–43.